

# **Vertical Momentum Transport over Mountainous Terrain**

By  
G.L. Wooldridge

Department of Atmospheric Science  
Colorado State University  
Fort Collins, Colorado



**Department of  
Atmospheric Science**

Paper No. 164

VERTICAL MOMENTUM TRANSPORT  
OVER MOUNTAINOUS TERRAIN

by  
Gene L. Wooldridge

This report was prepared with support  
under Contract Number NAS 9-10305  
National Aeronautics and Space Administration  
Principal Investigator, E. R. Reiter

Department of Atmospheric Science  
Colorado State University  
Fort Collins, Colorado

September, 1970

Atmospheric Science Paper No.164

## ABSTRACT

High-resolution pictures obtained with a handheld camera during the earth-orbital photographic mission of the Apollo IX spacecraft provided a unique opportunity to map the areal extent of gravity waves over the southwestern United States. The orientation of cumulus streets and cirrus streaks augmented conventional wind data for momentum and kinetic energy calculations.

Zonal shearing stress gradients in stably stratified air flowing over rugged mountainous terrain indicated very large subgrid-scale vertical fluxes of zonal momentum. Maximum stress values of several tens of dynes  $\text{cm}^{-2}$  occurred in the lower tropospheric layers where the air flow encountered the high Rocky Mountains of central New Mexico. The vertical fluxes of zonal momentum were directed upward to tropopause levels when extensive areas of gravity waves covered eastern Arizona, New Mexico, and western Texas.

The potential energy contained in the wave population attained values through the troposphere as high as  $9.3 \times 10^5$  joules  $\text{m}^{-2}$  ( $9.3 \times 10^8$  ergs  $\text{cm}^{-2}$ ); this potential energy apparently played a substantial role in the energy budget. The residual "dissipation" term in the kinetic energy budget indicated a subgrid-scale flux of energy downward from the lower stratosphere concurrent with the upward flux of zonal momentum. Atmospheric turbulence rose to a maximum intensity during the wave occurrence, diminishing gradually thereafter.

### ACKNOWLEDGEMENTS

The author gratefully acknowledges the patient guidance and encouragement of his adviser, Dr. E. R. Reiter, during the preparation of the work described here. Dr. W. M. Gray provided helpful suggestions and a critical review of the manuscript. Mr. Robert Gobin aided in the data reduction; Mr. R. Derickson handled the computer processing. Mrs. V. Sukumoljuntra typed the final manuscript.

This research was sponsored by the National Aeronautics and Space Administration under Contract Number NAS 9-10305, "The Meteorological Applications of Apollo Photography".

This material is based on a dissertation submitted as partial fulfillment of the requirements for the Doctor of Philosophy degree at Colorado State University.

## TABLE OF CONTENTS

	<u>Page</u>
TITLE PAGE.....	i
ABSTRACT.....	ii
ACKNOWLEDGEMENTS.....	iii
LIST OF TABLES.....	vi
LIST OF FIGURES.....	vii
I. INTRODUCTION.....	1
Horizontal Transport.....	1
Vertical Transport.....	2
Mountain Effects.....	4
Transport Mechanisms.....	5
Purpose of the Investigation.....	6
II. DESIGN OF THE EXPERIMENT.....	7
Data Sources.....	7
Region of Study.....	7
Data Treatment.....	9
Apollo IX Data.....	10
Grid Fitting.....	17
Synoptic Situation.....	19
III. ZONAL STRESSES AND ANGULAR MOMENTUM.....	30
Stress Computation.....	32
Zonal Shearing Stresses.....	34
Angular Momentum Budgets.....	44
IV. VORTICITY BUDGETS.....	47

TABLE OF CONTENTS - Continued

	Page
V. KINETIC ENERGY GENERATION AND DISSIPATION.....	52
Kinetic Energy Computational Results.....	53
Frictional Dissipation in Isentropic Coordinates...	61
VI. INTERPRETATION OF COMPUTATIONAL RESULTS.....	65
Zonal Shearing Stresses.....	71
Kinetic Energy and the Energy Cycle.....	73
Potential Energy of Waves.....	75
Dissipation of Wave Energy.....	80
VII. SUMMARY AND CONCLUSIONS.....	83
Summary.....	83
Conclusions.....	84
LITERATURE CITED.....	86

LIST OF TABLES

<u>Table</u>	<u>Page</u>	
3.1	Summary of angular momentum terms. Units for the individual levels are $10^3 \text{ m}^2 \text{ sec}^{-2}$ ( $10^7 \text{ cm}^2 \text{ sec}^{-2}$ ); units for the totals (integrated over pressure) are $10^6 \text{ kgm sec}^{-2}$ ( $10^9 \text{ gm sec}^{-2}$ ).....	42
3.1	Continued.....	43
4.1	Summary of vorticity terms. Units for the individual levels are $10^{-9} \text{ sec}^{-2}$ ; units for the totals (integrated over pressure) are $10^{-6} \text{ sec}^{-2}$ .....	49
5.1	Summary of kinetic energy terms. Units for the individual levels are $10^{-3} \text{ m}^2 \text{ sec}^{-3}$ ( $10 \text{ cm}^2 \text{ sec}^{-3}$ ); units for the totals (integrated over pressure) are watts $\text{m}^{-2}$ .....	54
5.1	Continued.....	55
5.2	Frictional dissipation in the free atmosphere.....	61
6.1	Energy residual over computational region.....	82

## LIST OF FIGURES

<u>Figure</u>		<u>Page</u>
2.1	Region of southwestern United States selected for application of stress and momentum relationships. Computational grid points and computational area are identified by crosses and solid lines. Circles are rawinsonde stations.....	8
2.2	Apollo IX handheld camera photograph No. 3446, taken at approximately 1805 GMT March 9, 1969. The earth's horizon can be seen at the upper portion of the picture. Extensive cirrus streaks can be seen through the center of the photograph (see A).....	11
2.3	Apollo IX handheld camera photograph No. 3441, taken at approximately 1804 GMT March 9, 1969. Cirrus streaks appear in the area north of B. The sharp cut-off from B to C coincides with the axis of the wind maximum at cloud level (about 500 mb).....	12
2.4	Apollo IX handheld camera photograph No. 3438, taken at approximately 1802 GMT March 9, 1969. A mesoscale cyclonic curvature is outlined in the cloud streaks at B. Extensive wave structure is visible at middle cloud level at A.....	13
2.5	Apollo IX handheld camera photograph No. 3443, taken at approximately 1804 GMT March 9, 1969. Long cumulus streets at about 12,000 ft MSL can be seen at B. Cirrus streaks are visible at A, extending eastward to 107W 37N.....	14
2.6(a)	Wind data used for objective analysis for 1800 GMT March 8, 1969 at the 700 mb level. Barbs indicate velocity in meters per second. Indicators originating on stations are interpolated from rawinsonde data; those passing through stations are from pibals. Streaklines are derived from Apollo IX photographed cloud streets, bases 8,000 to 10,000 ft MSL.....	16
2.6(b)	Same as 2.6(a) except for 1800 GMT March 9, 1969, at the 500 mb level. Streaklines are derived from cloud streaks at 19,000 to 23,000 ft MSL.....	16
2.7	Vertical layer structure used for momentum, stress gradient, energy, and vorticity budget calculations.	18

List of Figures Continued

<u>Figure</u>		<u>Page</u>
2.8	Height contours in tens of meters for 1800 GMT March 8, 1969 interpolated 300 mb (above) and 500 mb (below) maps.....	20
2.9	Isotachs of zonal wind in meters per second for 1800 GMT March 8, 1969 interpolated 300 mb (above) and 500 mb (below) maps.....	21
2.10	Height contours in tens of meters for 1800 GMT March 9, 1969 interpolated 300 mb (above) and 500 mb (below) maps.....	22
2.11	Isotachs of zonal wind in meters per second for 1800 GMT March 9, 1969 interpolated 300 mb (above) and 500 mb (below) maps.....	23
2.12	Height contours in tens of meters for 1800 GMT March 10, 1969 interpolated 300 mb (above) and 500 mb (below) maps.....	24
2.13	Isotachs of zonal wind in meters per second for 1800 GMT March 10, 1969 interpolated 300 mb (above) and 500 mb (below) maps.....	25
2.14	Height contours in tens of meters for 1800 GMT March 11, 1969 interpolated 300 mb (above) and 500 mb (below) maps.....	26
2.15	Isotachs of zonal wind in meters per second for 1800 GMT March 11, 1969 interpolated 300 mb (above) and 500 mb (below) maps.....	27
2.16	Height contours in tens of meters for 1800 GMT March 12, 1969 interpolated 300 mb (above) and 500 mb (below) maps.....	28
2.17	Isotachs of zonal wind in meters per second for 1800 GMT March 12, 1969 interpolated 300 mb (above) and 500 mb (below) maps.....	29
3.1	Vertical profiles of $\frac{\delta \bar{\tau}_x}{\delta p} \Delta p$ in units of $\text{kgm m}^{-1} \text{sec}^{-2}$ per 100 mb, or $\frac{\delta \bar{\tau}_x}{\delta p}$ in $10^{-4}$ , at 1800 GMT for days indicated. The pronounced reversal of profile occurred between March 8 and March 9, 1969.....	35

List of Figures Continued

<u>Figure</u>		<u>Page</u>
3.2	Vertical profiles of mean stresses ( $\overline{\tau_x}$ ) in units of $\text{kgm m}^{-1} \text{sec}^{-2}$ for 1800 GMT for days indicates. The directions of small-scale fluxes of zonal momentum are indicated by arrows. Multiply by 10 to obtain dynes $\text{cm}^{-2}$ .....	35
3.3	Individual terms in the zonal stress gradient computation. The dotted line is the inertial term $du/dt$ ; dashed line is $g^{\partial z/\partial x}$ ; dot-dashed line is the Coriolis term $(-fv)$ ; solid line is $F_x$ , or $-g^{\partial \tau_x/\partial \rho}$ . Units are $10^{-4} \text{ m sec}^{-2}$ ( $10^{-2} \text{ cm sec}^{-2}$ )...	36
3.4(a) and (b)	Contours of zonal stress ( $\tau_x$ ) for 1800 GMT March 8, 1969 at the 300 mb and 400 mb levels. Units are $\text{kgm m}^{-1} \text{sec}^{-2}$ . Multiply by 10 to obtain dynes $\text{cm}^{-2}$ .	38
3.4(c) and (d)	Same as Figures 3.4(a) and (b) except for 500 mb and 700 mb.....	39
3.5(a) and (b)	Contours of zonal stress ( $\tau_x$ ) for 1800 GMT March 9, 1969 at the 300 mb and 400 mb levels. Units are $\text{kgm m}^{-1} \text{sec}^{-2}$ . Multiply by 10 to obtain dynes $\text{cm}^{-2}$ .	40
3.5 (c) and (d)	Same as Figures 3.5(a) and (b) except for 500 mb and 700 mb.....	41
3.6	Vertical profiles for angular momentum terms for March 8 through 12, 1969. Units are $10^3 \text{ m}^2 \text{sec}^{-2}$ ( $10^7 \text{ cm}^2 \text{sec}^{-2}$ ).....	46
4.1	Vertical profiles for vorticity budgets for March 8 and 9, 1969. Units are $10^4 \text{ kgm sec}^{-2}$ per mb, or $10^{-9} \text{ sec}^{-2}$ .....	50
5.1	Vertical profiles for kinetic energy budget terms for March 8 through 12, 1969. Units are $10^{-3} \text{ m}^2 \text{sec}^{-3}$ ( $10 \text{ cm}^2 \text{sec}^{-3}$ ).....	56
5.2	Vertical profiles of the mean zonal wind velocity for the region of study in meters $\text{sec}^{-1}$ . The solid line is for the entire region; the dashed line is for the western boundary; the dot-dashed line is for the eastern boundary.....	57
5.3(a) and (b)	Streamline analysis for 700 mb (a) and 500 mb (b) for 1800 GMT March 8, 1969.....	58

List of Figures Continued

<u>Figure</u>	<u>Page</u>
5.4(a) Streamline analysis for 700 mb (a) and 500 mb (b) and (b) for 1800 GMT March 10, 1969.....	59
5.5 Vertical profiles of stress ( $\bar{\tau}_{x,\theta}$ ) in units of kgm m <sup>-1</sup> sec <sup>-2</sup> for 0000 GMT on days indicated, computed in isentropic coordinates. Multiply by 10 to obtain dynes cm <sup>-2</sup> .....	63
6.1(a) Streamline analysis for flow in the lowest 100 mb and (b) of the atmosphere for 0000 GMT March 9 (a) and March 10 (b), 1969.....	70
6.2 Apollo IX photograph No. 3447, taken at approxi- mately 1804 GMT March 9, 1969. Lee wave clouds are visible at A; a cap cloud covers the mountain ridge at B.....	76
6.3 Apollo IX photograph No. 3294, taken at approxi- mately 1805 GMT March 9, 1969. Wave clouds at A are in the Lee of the mountains; billows at B are superimposed on the longer waves.....	77
6.4(a) Winslow, Arizona sounding for 1200 GMT March 9, 1969. The solid line is temperature; dashed line is dew point temperature. Wind barbs indicate velocity in knots.....	78
6.4(b) Same as 6.4(a), except for Albuquerque, New Mexico.....	78

## DEFINITION OF SYMBOLS

### English Letters

$a$	radius of the earth
$A$	area of horizontal surface
$c_n$	velocity normal to surface, positive outward.
$\frac{d}{dt}$	individual derivative with respect to time
$D$	frictional dissipation of kinetic energy to heat.
$f$	Coriolis parameter
$\vec{F}_2$	two-dimensional shearing stress force
$F_x$	zonal shearing stress force
$F_y$	meridional shearing stress force
$g$	acceleration due to gravity
$\vec{i}$	unit vector positive eastward
$\vec{j}$	unit vector positive northward
$K$	horizontal kinetic energy
$\ell$	subscripted, the lower bounding surface
$L$	peripheral length of computation region
$M$	absolute angular momentum
$p$	pressure
$p_i$	given pressure level
$r$	perpendicular distance from earth's axis to the earth's surface
$u$	zonal wind velocity, positive eastward
$u_g$	geostrophic zonal wind velocity
$u'$	perturbation zonal wind velocity
$U$	mean zonal wind velocity

## Definition of Symbols Continued

### English Letters

$v$	meridional wind velocity, positive northward
$v_g$	geostrophic meridional wind velocity
$v'$	perturbation meridional wind velocity
$\vec{V}_3$	three-dimensional wind vector
$\vec{V}_2$	two-dimensional wind vector
$w'$	perturbation vertical velocity
$x$	distance along coordinate axis, positive eastward
$y$	distance along coordinate axis positive northward
$z$	vertical displacement from surface
$z'$	vertical perturbation displacement

### Greek Letters

$\gamma$	coefficient of piezotropy
$\Gamma$	coefficient of piezotropy, equilibrium state
$\frac{\partial}{\partial t}, \frac{\partial}{\partial x}, \frac{\partial}{\partial y}, \frac{\partial}{\partial z}$	partial derivative with $t, x, y, z$ respectively
$\nabla_3$	three-dimensional del operator
$\nabla_2$	two-dimensional del operator
$\epsilon$	viscous dissipation of energy to heat
$\zeta$	relative vorticity above the vertical axis
$\theta$	potential temperature
$\lambda$	longitude
$\nu_0$	Brunt-Väisälä frequency
$\pi$	3.1416
$\rho$	density of atmosphere

## Definition of Symbols Continued

### Greek Letters

$\tau_x, \tau_y$	shearing stresses in zonal and meridional direction, respectively.
$\phi$	latitude
$\omega$	defined = $dp/dt$
$\Omega$	angular rotation rate of the earth

## I. INTRODUCTION

An understanding of the structure and maintenance of the atmospheric circulation requires a knowledge of the horizontal and vertical transports of relative angular momentum (Palmén and Newton, 1969). Early computations of horizontal transports revealed a general northward movement directed from the upper level westerlies in the subtropics to the midlatitude westerlies (Widger, 1949; Lorenz, 1951). These computations implied an upward flux of angular momentum from the low-level subtropic belt of easterlies and a net downward movement over temperate latitudes. The dividing line between surface westerlies in the northern hemisphere mid-latitudes and the surface easterlies to the south proves to be an area of special interest for angular momentum studies (Starr and White, 1951).

### Horizontal Transport

Considerable literature exists on the horizontal eddy transport mechanisms which can bring about the northward flux of relative angular momentum, including studies by Starr (1951), Starr and White (1951, 1952a, 1952b), Lorenz (1952), and Gilman (1964). The horizontal transient eddy transport against the gradient of zonal momentum suggests the possibility that vertical eddy flux can also take place against the vertical gradient of angular momentum in the transition region. Further, the difficulty in establishing a significant mean meridional mass circulation on the required order of one meter per second in the

horizontal indicates a major role for eddy transport in the general atmospheric circulation.

### Vertical Transport

In addition to the sizeable contribution by eddies on various length scales to the horizontal redistribution of angular momentum, the vertical flux of momentum may be largely due to eddies on many scales, from the planetary wavelengths to small-scale shearing stresses (Reiter, 1969). The large-scale mean vertical transport by mass flux has been measured for extended periods of time (Palmén, 1966; Oort and Rasmusson, 1970). The vertical momentum flux can be estimated by assigning an arbitrary surface drag coefficient to a friction torque term (Widger, 1949), but in hemispheric mean calculations this leads to inconclusive values in a momentum budget. Starr and Dickinson (1964) measured the standing and transient eddy vertical transport of relative angular momentum on the large scale using standard meteorological data; they found opposing signs for winter and spring vertical momentum transfer over the northern hemisphere (averaged 20N to 80N) and concluded that the large-scale vertical eddies act to decrease upper level zonal flow in January and to increase it in April. Lorenz (1967) has suggested that the net effects of large scale eddies are ineffective in vertical momentum transport, and that the vertical transport requirements may be mainly accomplished by the mean circulation of the meridional cells.

The vertical eddy transport on various length scales led Gilman (1964) to conclude that those length scales not visible in the conventional rawinsonde network may at times move momentum in a direction opposite to that of large scales near the tropopause region.

Measurements of "negative eddy viscosity" near the midlatitude jet stream were interpreted by Gilman as evidence that near the jet the net effect of vertical eddies of all scales brought about momentum transport into the jet stream. Negative eddy viscosity results when eddy momentum flux is directed from regions of low mean flow values to regions of higher values, acting in the reverse direction of frictional drag. Kung (1967) also found "negative viscosity" in tropopause regions in the annual mean kinetic energy budgets over North America. If eddies transport momentum upward, a constant downward transport by mean flow must occur to bring about a total net downward flux to balance the hemispherical requirements for a sink in midlatitudes. This mean vertical motion was measured by Jensen (1961) for January 1958 on the order of a few tenths of a centimeter per second, by Saltzman and Fleisher (1960) for February 1959 as about one-tenth of a centimeter per second and more recently from .5 to .8 cm sec<sup>-1</sup> by Oort and Rasmusson (1970). Jensen speculated that the "negative dissipation" calculated at tropopause levels for January 1958 might be explained by a generation of kinetic energy in eddies on a scale not detected in the conventional meteorological data network.

Priestley (1967) indicated that vertical flux of angular momentum in the temperate belt of westerlies was possible in synoptic scale disturbances, mesoscale motions, and smaller scales. He suggested that existing steady-state treatments required modification on the basis of time variation. In an earlier discussion Priestley (1959) indicated that Reynolds stresses above the planetary boundary layer probably played a significant part in the general circulation of the atmosphere,

and that a study of terrain drag would be preferred to site studies; over land this distinction may be important.

These stresses above the lowest 1 km of the atmosphere include (1) true viscous drag forces which dissipate heat and have an effect on the total heat budget in the free atmosphere and (2) vertical fluxes of momentum, either upward or downward. The combined effects of vertical redistribution of momentum and viscous dissipation to heat may serve to integrate the effect of small scale phenomena into the larger scales.

#### Mountain Effects

The effects of mountain ranges in temperate latitudes have been calculated by White (1949), Riehl and Baer (1964), and Kung (1968) among others. Riehl and Baer showed that the mountainous region of North America between 30N and 60N played an important role in the vertical momentum exchange between the earth and the atmosphere. Further, they found that the momentum exchange could take place either upward or downward. Kung (1968) found that the mountain effect

$$\left( \bar{m} = \frac{1}{2\pi a \cos\phi} \int_0^H \Delta p dz \right)$$

was a significant term in the momentum exchange and on the same order as the friction torque effect

$$\left( \bar{\tau}_{ox} = \frac{1}{2\pi a \cos\phi} \oint \rho C_2 u^2 dx \right)$$

when calculations were made on the scale of the standard data network. In Kung's terms,  $a$  is the radius of the earth,  $\Delta p$  the pressure difference across a mountain whose highest peak has the height  $H$ ,  $\rho$  is the

atmospheric density,  $u_g$  is the zonal component of the geostrophic wind, and  $C$  is the geostrophic drag coefficient. In the 30N-40N latitude belt, the ratio of the mountain effect to the stress effect was 5.2 in the annual mean; at 40N-50N it was 0.6. On an annual basis, the surface stress was negative at 30N; in the 35N-40N latitude belt the stress was positive but smaller in magnitude. A wide range of stress values has been computed, suggesting that regional descriptions of this parameter obtained through detailed studies are important for prescribing proper values for numerical analyses and experiments.

#### Transport Mechanisms

Rossby (1951) noted that the westerly winds entering the west coast of the United States often experienced an acceleration and a change in vertical structure while traversing the mountains. Rossby concluded that the vertical stability distribution played an important part in the concentration of momentum in shallow layers of air, resulting in sharp jets in stratified air; further, that eddy momentum transfer, large in comparison to the diffusion of mass properties, established a limiting vertical wind profile characterized by a rapid increase in speed and vertical stability with height. If the vertical eddy redistribution of relative angular momentum into upper layers took place at the expense of lower layers, a corresponding sharpening of the horizontal flow profile followed due to the decrease in velocity in the lower levels.

The role of vertical momentum transport by convective eddies in the suppression of the vertical shear of the horizontal wind has been discussed by Gray (1968). Gray showed that the up- and downdrafts

could act to decrease the wind shear at the same time that the baroclinicity increased during the initial generation of a cyclonic disturbance; the resulting friction disturbed the geostrophic balance.

This convective-scale turbulence involves mass transport which vertically redistributes passive properties of the atmosphere as well as momentum in convectively unstable conditions. The vertical transfer of relative angular momentum by convective motions can be very large during summer periods, when a single well-developed squall line can account for 30-40% of the total requirement for vertical transport of momentum for a 20-degree latitude belt. However, there are extensive areas over which no cumulonimbi can be found during the winter season, when hemispheric requirements for vertical transfer are greater than in summer. It seems unlikely that convective turbulence in a stable extra-tropical region can account for the necessary vertical redistribution over continents in winter (Palmén and Newton, 1969).

#### Purpose of the Investigation

The research conducted here investigates the hypothesis that significant subsynoptic-scale vertical transport of relative angular momentum can take place over mid-latitude mountainous terrain in a stably-stratified atmosphere through the action of extensive areas of internal gravity waves. The research additionally investigates the possibility that this small-scale vertical redistribution can be directed upward into tropopause levels to maintain a high-velocity wind maximum against frictional dissipation.

## II. DESIGN OF THE EXPERIMENT

### Data Sources

The reliability of the calculation of vertical momentum fluxes, or shearing stresses, depends on the accuracy of the required meteorological data. These data consist of the height of the pressure surfaces and the wind direction and velocity. The conventional collection system provides rawinsonde information on these parameters on the synoptic scale at 0000 GMT and 1200 GMT and, at a few stations, also at 0600 GMT and 1800 GMT. The low-level data density is increased at 1800 GMT through pilot balloon soundings.

Wind directions deduced from cloud streets and streaks (Kuettner, 1959) photographed by the Apollo IX astronauts augment the 1800 GMT data. The 1800 GMT time was primarily chosen for study to make use of the subsynoptic-scale information recorded in the earth-oriented Apollo pictures taken during the March 8-12, 1969 time period. Center differencing for local time changes at 1800 GMT utilized the 1200 GMT data for the same day and the 0000 GMT data for the following day; this allowed the use of actual data for a 12-hour time interval.

### Region of Study

The presence of high, rugged terrain, the regular spacing of rawinsonde station locations, and the coverage by high-resolution Apollo IX photography determined the region selected for study. The period of study encompassed the earth-oriented photographic mission of the Apollo crew. The area outlined in Figure 2.1 in solid lines constituted the region, covering about  $10^{12} \text{ m}^2$  in Arizona, New Mexico, and parts of western Texas and Oklahoma. Mountain peaks in eastern

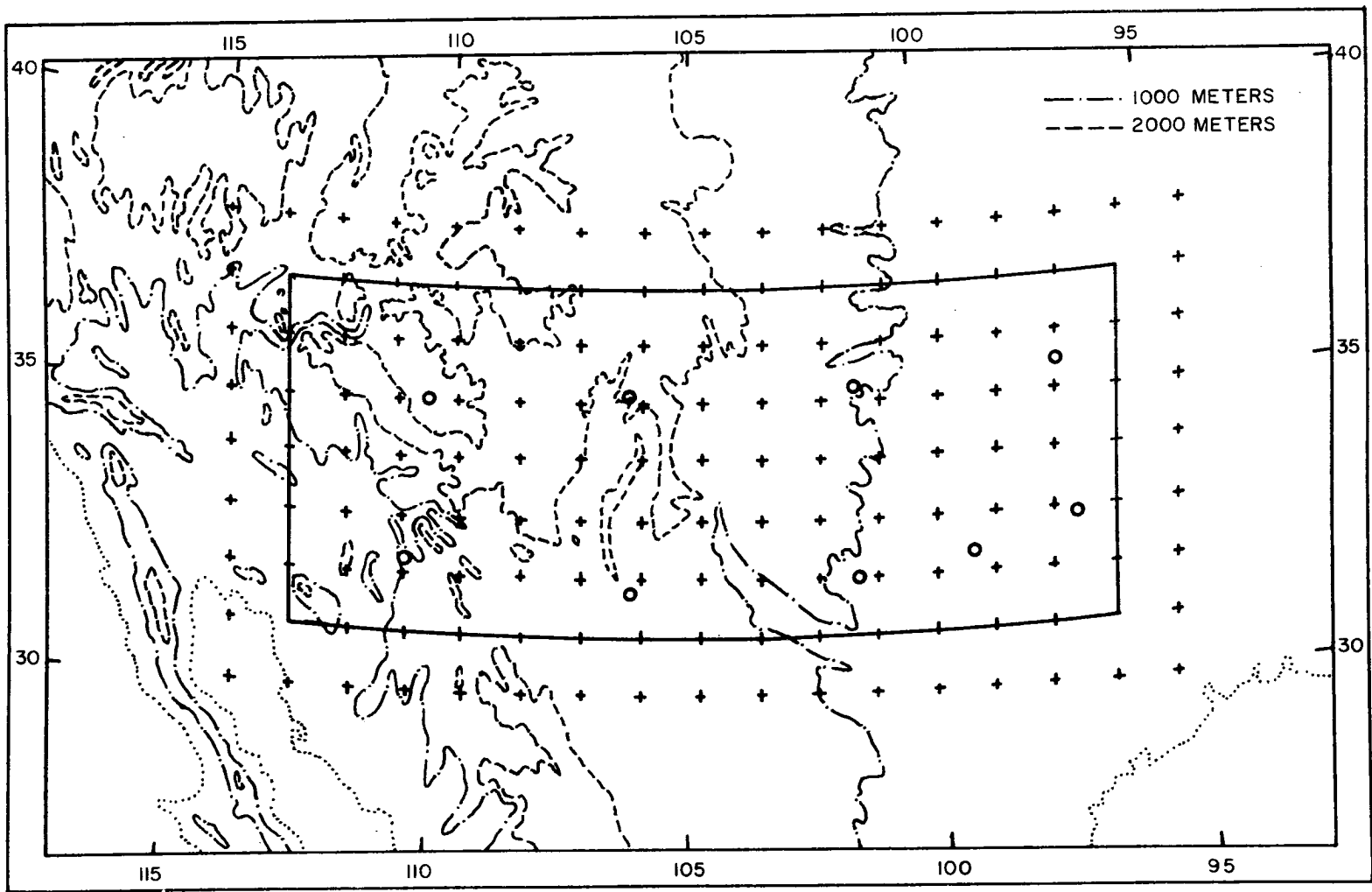


Figure 2.1. Region of southwestern United States selected for application of stress and momentum relationships. Computational grid points and computational area are indicated by crosses and solid lines. Circles are rawinsonde stations.

New Mexico rise to 4 km, with numerous elevations over 3 km in Arizona and New Mexico. The ridges are irregularly spaced and oriented, allowing interaction between the perturbations imposed on the airflow passing over the terrain. The frequent occurrence of clear air turbulence (Reiter and Foltz, 1967) reflects the generation and interaction of mountain waves over the region. The region is also an area over which the jet stream is frequently located (Lester, 1969).

#### Data Treatment

The March 8-13, 1969, 0000 GMT and 1200 GMT rawinsonde data for the nine stations within and for sixteen stations surrounding the region were first reduced to u- and v-components. The time series of the standard pressure heights and the wind components were then subjected to a cubic "spline" curve fitting and interpolation technique to extract 1800 GMT data.

The one-dimensional spline program (Fowler and Wilson, 1966) fits a normalized cubic polynomial curve to a set of points for each data time series (u- and v-components and pressure heights for standard levels). This spline curve features continuous position, slope, and curvature. If no smoothing is applied, the curve passes exactly through the given set of data points; smoothing of the curve is optional. For the work performed in this study, smoothing was not applied. Intermediate data values for 1800 GMT subsequently were interpolated from the continuous cubic curve passing through 0000 GMT and 1200 GMT rawinsonde data points, and these data added to the 1800 GMT pilot balloon data population within and immediately surrounding the study region.

### Apollo IX Data

The wind directions deduced from the orientation of cumulus streets and cirrus streaks in the photographs taken with the Apollo IX handheld cameras augmented the data assembled for 1800 GMT on March 8 through 12, 1969. A few examples exhibited here indicate the extent of the cloud streaks and streets photographed over the southwestern United States from the Apollo spacecraft. These cloud streets and streaks very nearly approximated the orientation of the air flow at cloud levels when the clouds had limited vertical dimension; when compared to conventional wind data from pilot balloons at the same level and geographic location the agreement was remarkably good. In areas where no pilot balloon data were available, cloud orientations were applied at the nearest standard pressure levels; the wind velocities were determined from pilot balloon and interpolated rawinsonde data.

Thin cirrus cloud streaks visible at A in Figure 2.2 stretched across the breadth of the Apollo photograph, a distance of about 350 km. Aircraft observations located these streaks at 22,000 ft MSL, slightly above the 500 mb level. These same cirrus streaks can be seen at B in Figure 2.3 in the 36-37N latitude belt. The northern edge of the heavier cloud ribbon identified in the center of Figure 2.3 coincided with the horizontal axis of the wind maximum at the 500 mb level.

The extensive wave populations photographed with the Apollo IX cameras indicated the presence of meso-scale gravity waves over a large portion of eastern Arizona, New Mexico, and western Texas. These waves were manifested in the clouds at stable atmospheric layers near 500 mb and 700 mb on March 9, 1969.

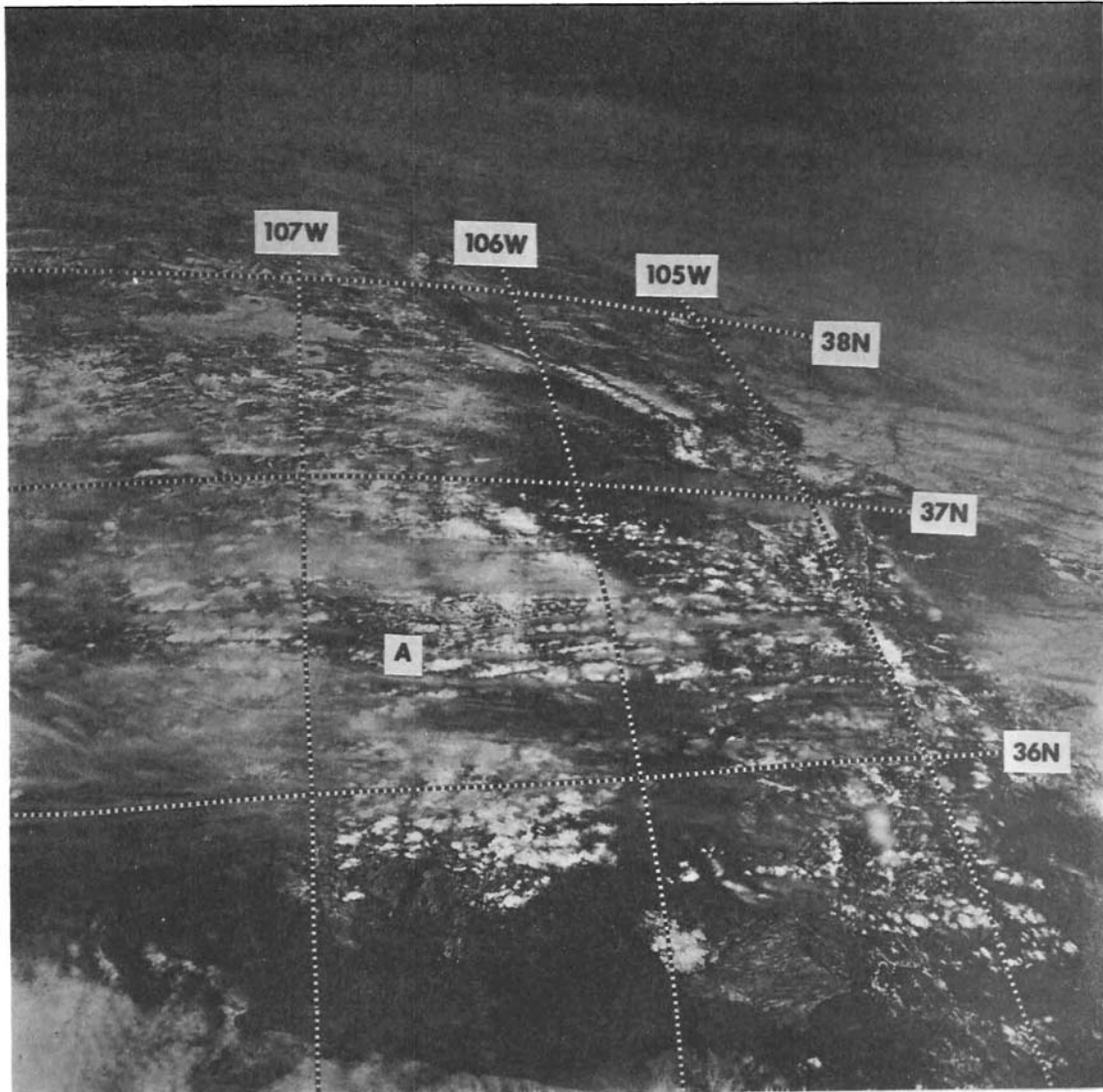


Figure 2.2. Apollo IX handheld camera photograph No. 3446, taken at approximately 1805 GMT March 9, 1969. The earth's horizon can be seen at the upper portion of the picture. Extensive cirrus streaks can be seen through the center of the photograph (see A).

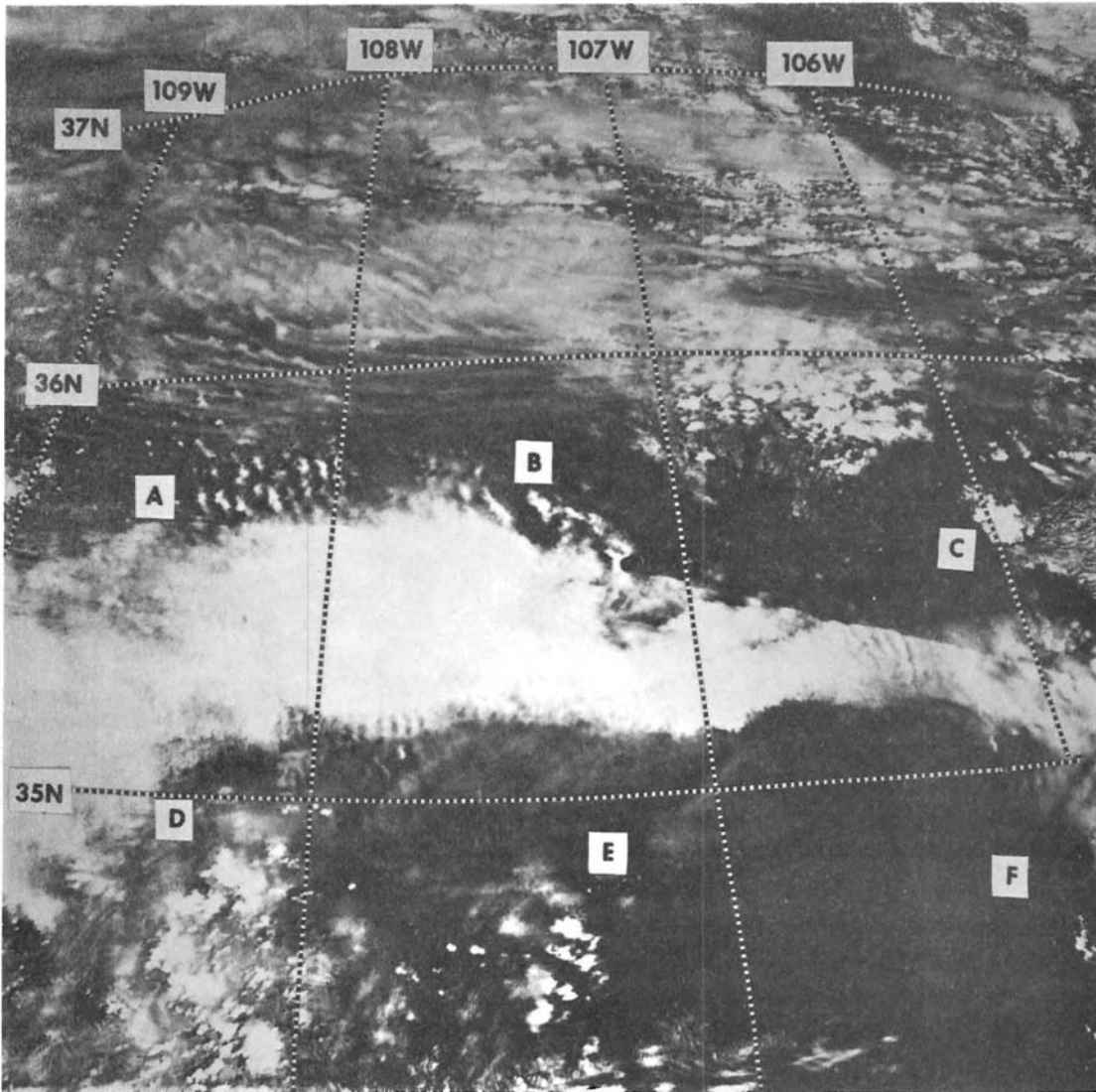


Figure 2.3. Apollo IX handheld camera photograph No. 3441, taken at approximately 1804 GMT March 9, 1969. Cirrus streaks appear in the area north of B. The sharp cut-off from B to C coincides with the axis of the maximum wind at cloud level (about 500 mb).

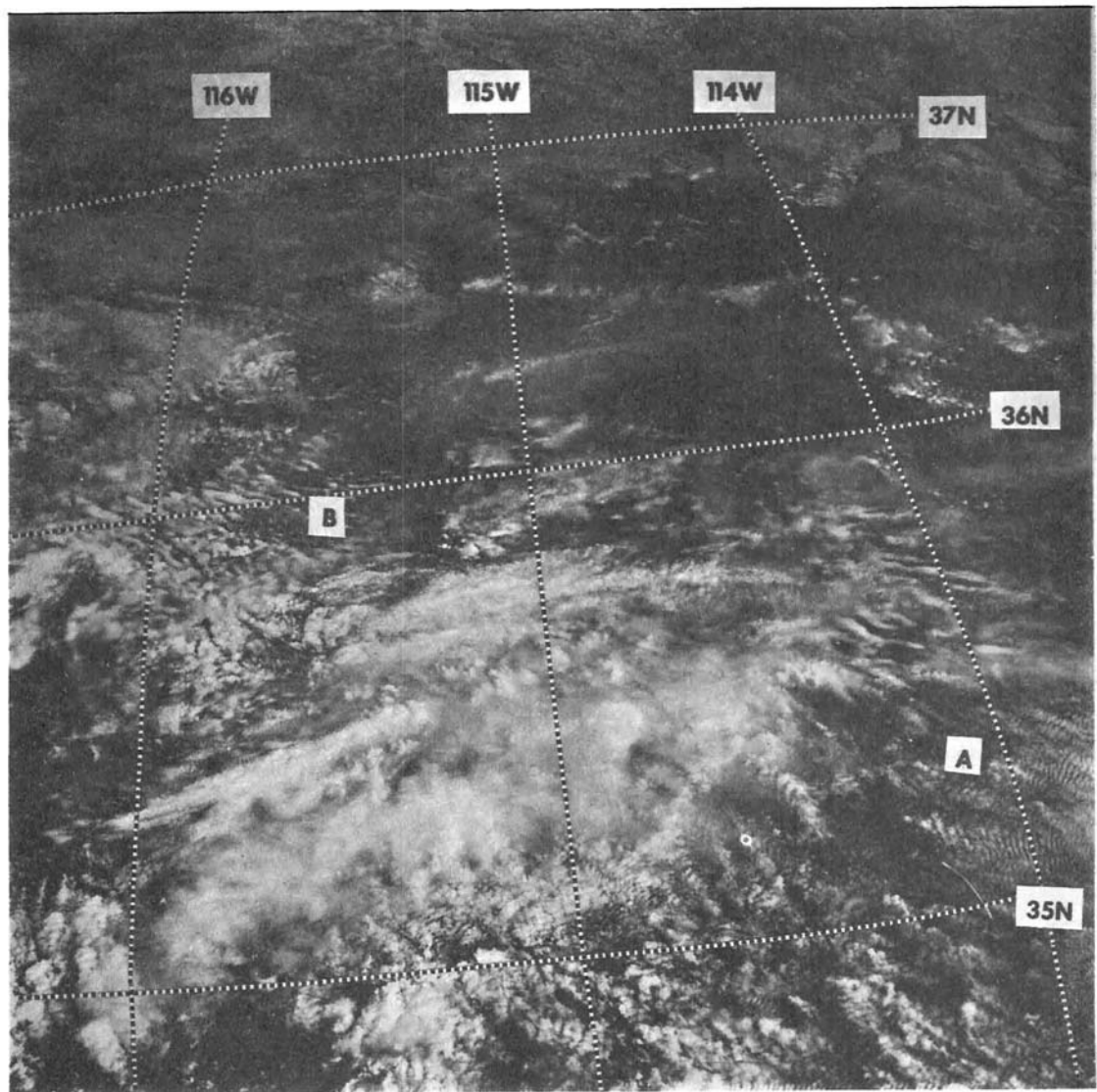


Figure 2.4. Apollo IX handheld camera photograph No. 3438, taken at approximately 1802 GMT March 9, 1969. A mesoscale cyclonic curvature is outlined in the cloud streaks at B. Extensive wave structure is visible at middle cloud level at A.

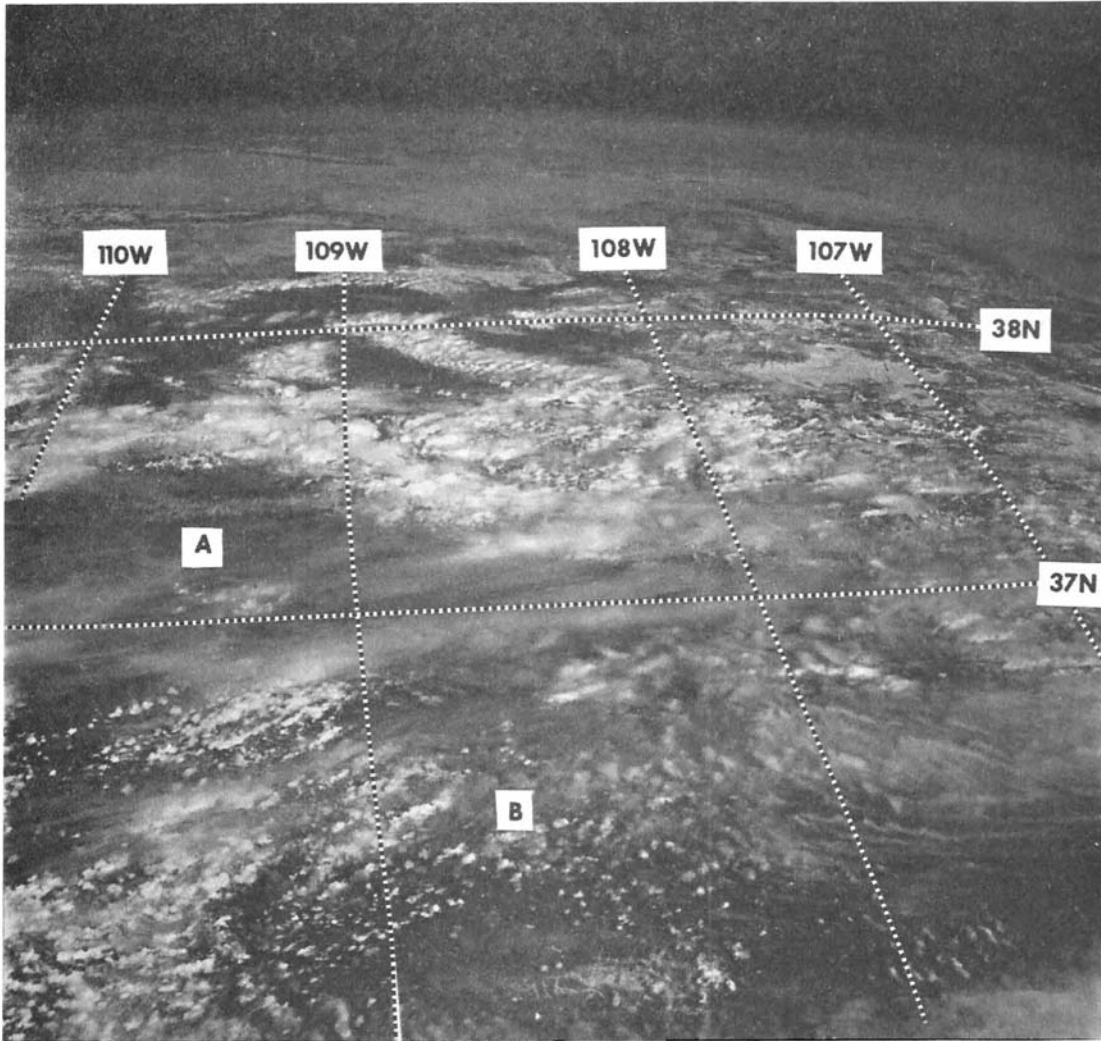


Figure 2.5. Apollo IX handheld camera photograph No. 3443, taken at approximately 1804 GMT March 9, 1969. Long cumulus streets at about 12,000 ft MSL can be seen at B. Cirrus streaks are visible at A, extending eastward to 107W 37N.

The clouds indicated at B in Figure 2.4 delineated the cyclonic curvature of the air flow at the 18,000 ft MSL, or approximately 500 mb, level. Cirrus streaks appeared at higher levels in the top part of the picture. Long cumulus streets in Figure 2.5 extended horizontally for about 180 km at an elevation of approximately 12,000 ft MSL, just above the 700 mb level.

The density and areal extent of the wind information extracted from the Apollo pictures, interpolated rawinsonde winds, and pilot balloons are exhibited in Figures 2.6(a) and (b) for 1800 GMT March 8 and 9, 1969, respectively. The arrows in Figure 2.6(a) represent the air-flow deduced from long rows of small cumuli with bases at 8,000 to 10,000 ft MSL and with tops, according to aircraft reports, near 13,000 ft MSL. The cloud streets were more closely spaced than required for the one-degree grid network and were concentrated in the mountainous regions of eastern Arizona and New Mexico. The cloud street orientation agreed closely with the directions of the rawinsonde and pilot balloon winds. The lengths of the streaklines approximate the lengths of the cloud streets in the Apollo IX photographs.

The same good agreement between streaklines and conventional data held for 1800 GMT March 9. The cloud heights recorded by aircraft and ground observers coincided with moist layers in the Winslow and Albuquerque soundings for 1200 GMT March 9. The curvature in the streakline north of Albuquerque identified a mesoscale horizontal perturbation in the airflow pattern. No Apollo photographs were available for March 10, and the reduction of the streakiness of the clouds on March 11 and 12 resulted in more sparse information on the airflow for those days.

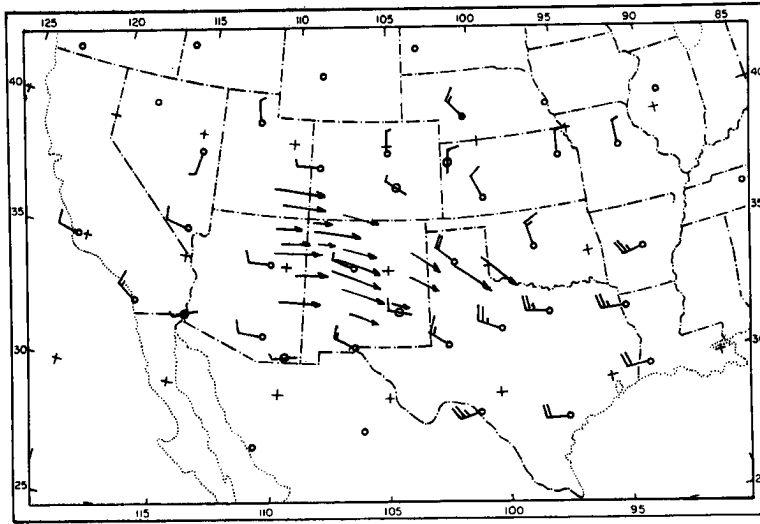


Figure 2.6(a). Wind data used for objective analysis for 1800 GMT March 8, 1969 at the 700 mb level. Barbs indicate velocity in meters per second. Indicators originating on stations are interpolated from rawinsonde data; those passing through stations are from pibals. Streaklines are derived from Apollo IX photographed cloud streets, bases 8,000 to 10,000 ft MSL.

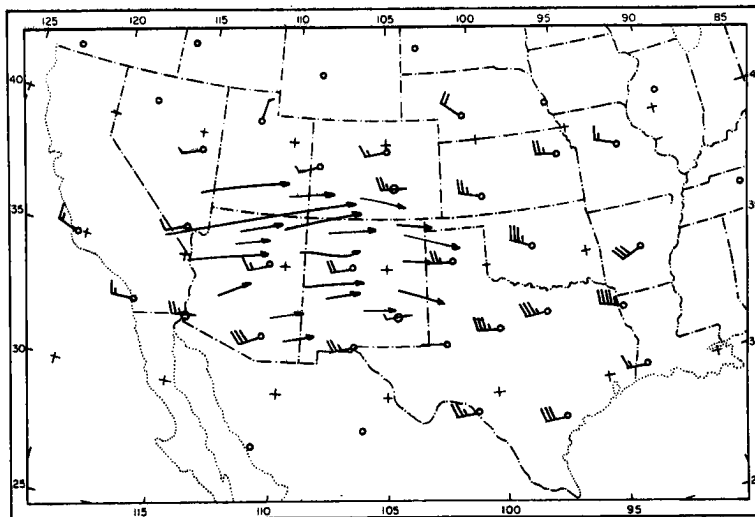


Figure 2.6(b). Same as 2.6(a) except for 1800 GMT March 9, 1969, at the 500 mb level. Streaklines are derived from cloud streaks at 19,000 to 23,000 ft MSL.

### Grid Fitting

The total data population from the rawinsonde time series, Apollo IX photographs, and pilot balloons, was objectively fitted to the grid shown in Figure 2.1. The longitudinal grid line is true at  $104^{\circ} 30'N$ , and grid lengths are  $1.111 \times 10^5$  m in the x- and y- directions (one latitude degree); the x-direction lies along latitude lines. The one-degree grid network yields a two-degree distance interval for center differencing in horizontal space.

In areas of extensive cloud streaking the extracted wind data were applied at grid points. The pilot balloon and interpolated rawinsonde data were fitted to the computational grid at standard pressure levels by a two-dimensional bicubic spline technique similar to that developed by Fritsch (1969). A sphere was fitted to the nearest four data values for each grid point; the grid point data values were compared with the mean values for the given level and parameter. If the difference was greater than two standard deviations a linear interpolation between the two nearest acceptable values was used at the point. All grid point values were again checked to see if they violated a maximum permissible slope at grid points. The entire data field was next smoothed in the two horizontal directions, allowing the grid points to converge to a surface. The smoothing could have reduced gradients near discontinuities or frontal surfaces, but no such events were involved in the cases selected for study here.

The spline analysis gave generally acceptable data fields for the u- and v- components of the wind, but required excessive smoothing for pressure heights. Consequently, heights interpolated from the time

series by the one-dimensional spline were subjectively analyzed, producing a hybrid objective-subjective analysis for the height fields.

The average computations for a given layer were assumed to hold for a layer centered at each standard pressure surface; the vertical structure is shown in Figure 2.7. The standard 100, 150, 300, 400, 500, and 700 mb pressure levels used are shown by solid lines; layer boundary surfaces are indicated by dashed lines. Nominal pressure thicknesses for each layer appear at the right-hand side.

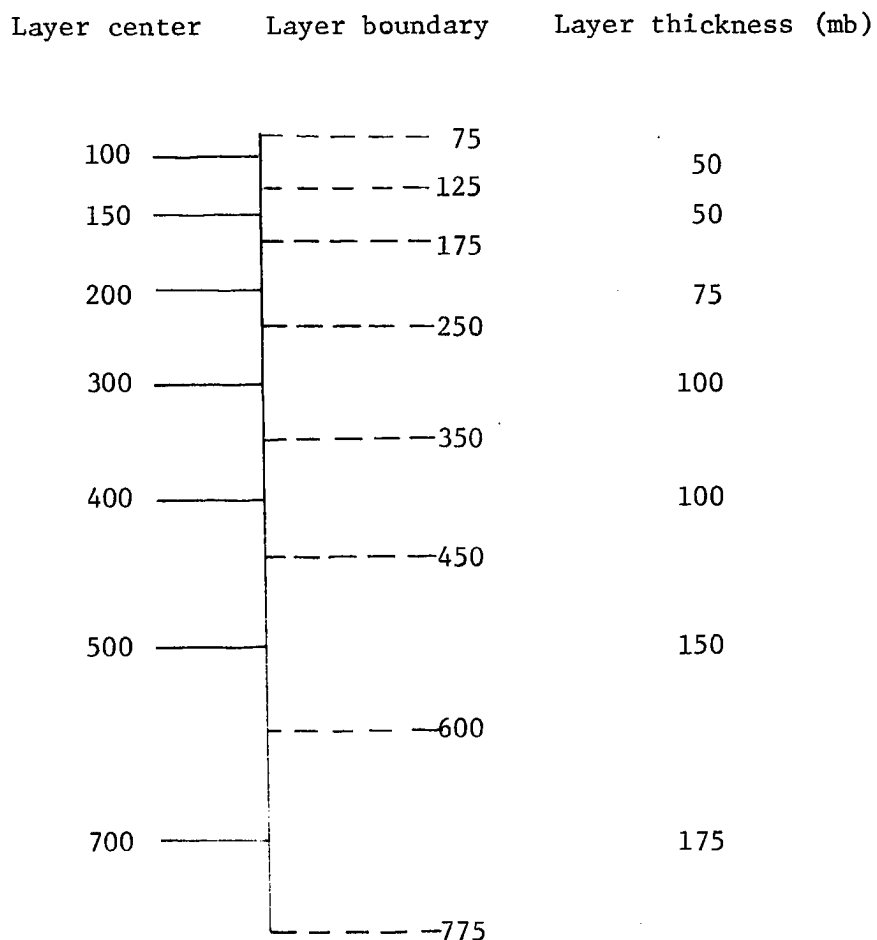


Figure 2.7. Vertical layer structure used for momentum, stress gradient, energy, and vorticity budget calculations.

### Synoptic Situation

The 500 mb and 300 mb 1800 GMT interpolated pressure-height contour (Figures 2.8, 2.10, 2.12, 2.14, and 2.16) and zonal wind isotach (Figures 2.9, 2.11, 2.13, 2.15, and 2.17) analyses indicate the nature of the middle and upper tropospheric flow for March 8 through 12, 1969. Sustained high zonal wind speeds in the upper troposphere characterized the period over which the calculations extended. A weak low-level cyclonic disturbance entered the western boundary of the study region March 10, traversed the northern portion March 11, and exited to the east March 12, 1969.

The fixed computational grid location was chosen to take advantage of good rawinsonde coverage, to contain the consistent high-velocity upper winds, and to cover the rugged terrain of Arizona and New Mexico. The axis of the jet stream was often contained in the grid.

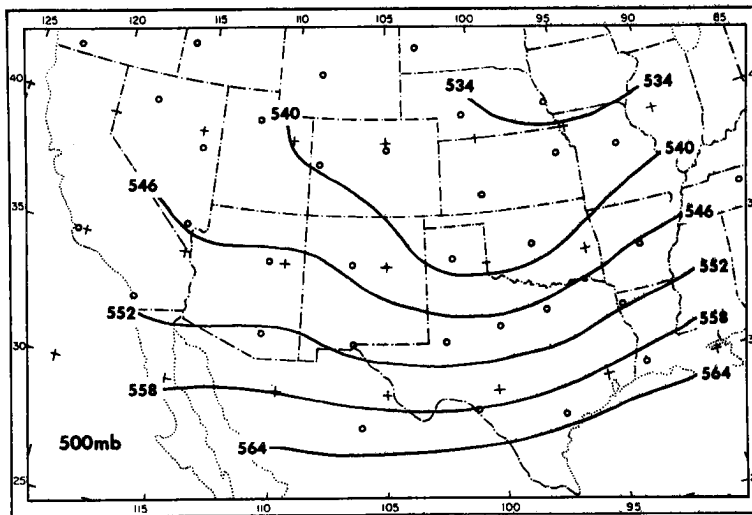
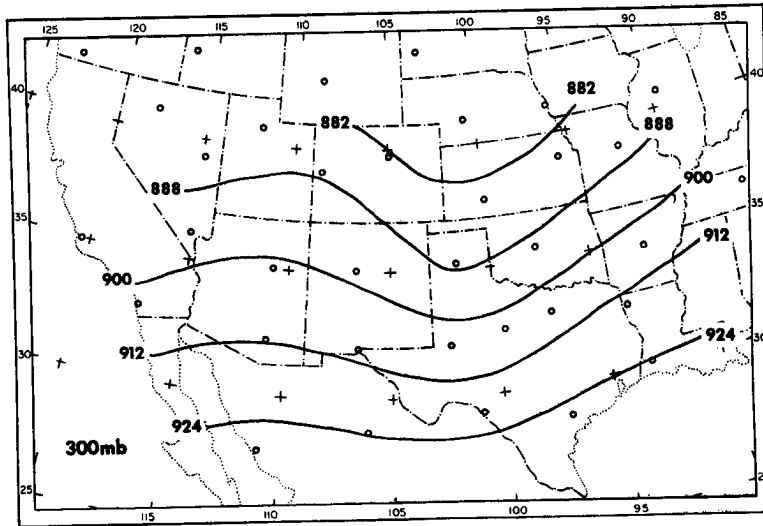


Figure 2.8. Height contours in tens of meters for 1800 GMT March 8, 1969 interpolated 300 mb (above) and 500 mb (below) maps.

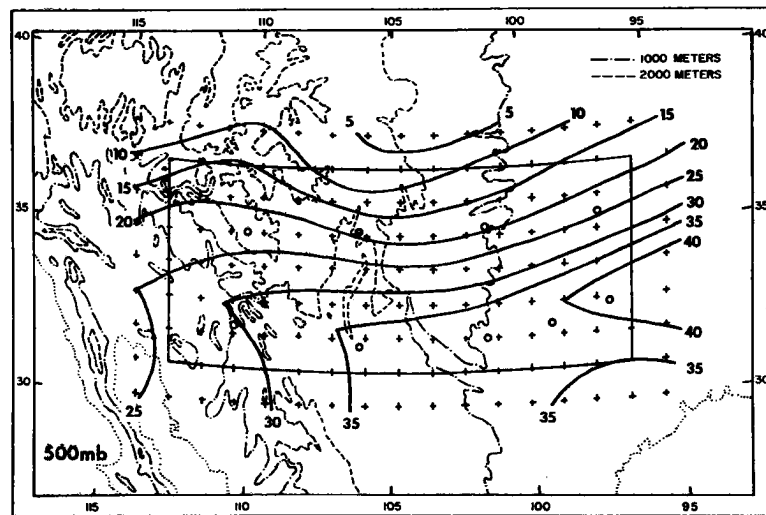
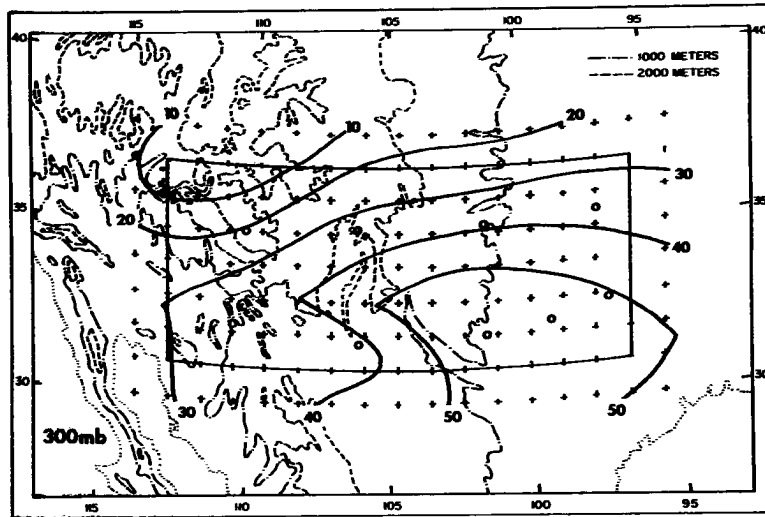


Figure 2.9. Isotachs of zonal wind in meters per second for 1800 GMT March 8, 1969 interpolated 300 mb (above) and 500 mb (below) maps.

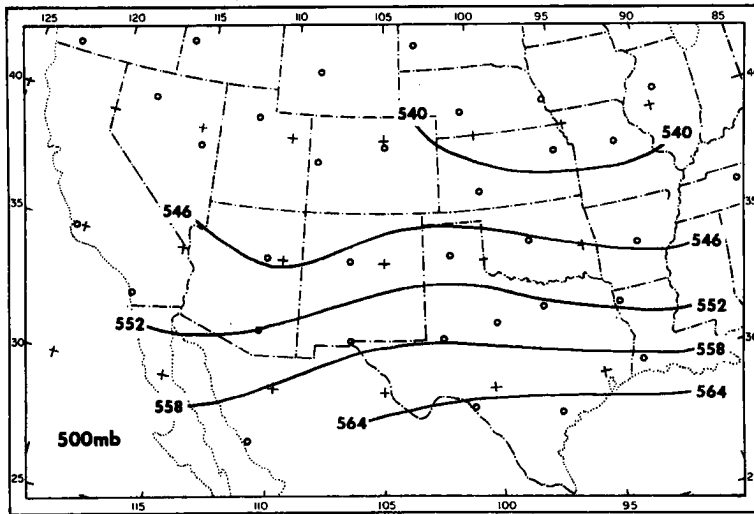
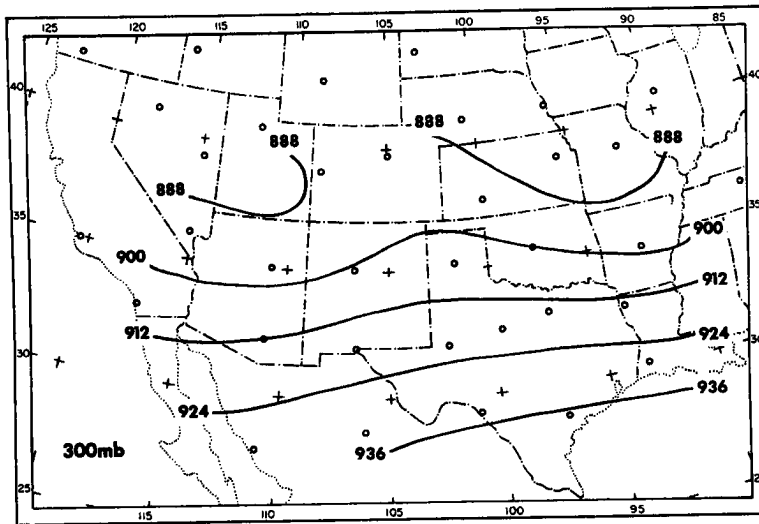


Figure 2.10. Height contours in tens of meters for 1800 GMT March 9, 1969 interpolated 300 mb (above) and 500 mb (below) maps.

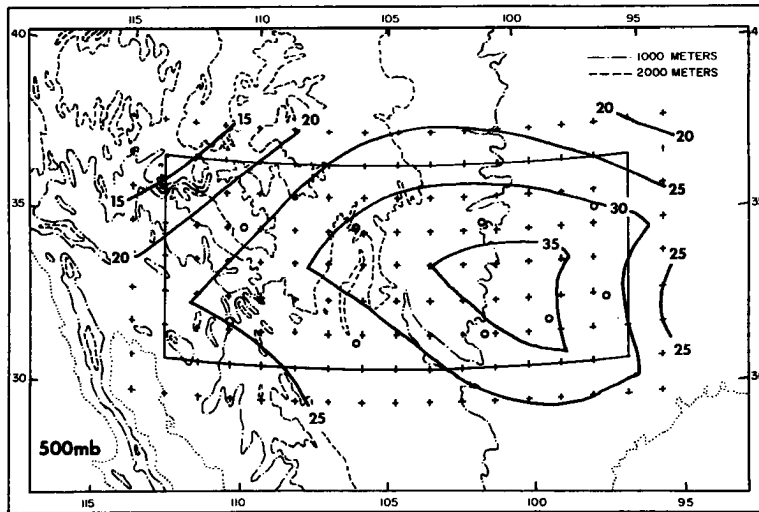
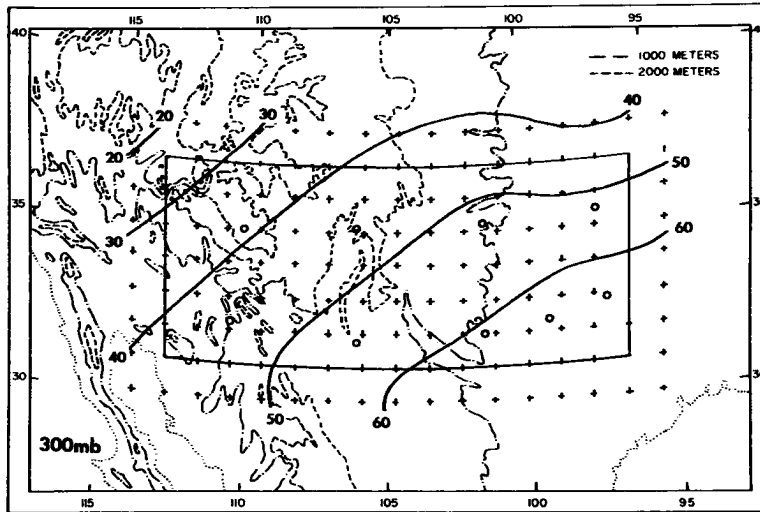


Figure 2.11. Isotachs of zonal wind in meters per second for 1800 GMT March 9, 1969 interpolated 300 mb (above) and 500 mb (below) maps.

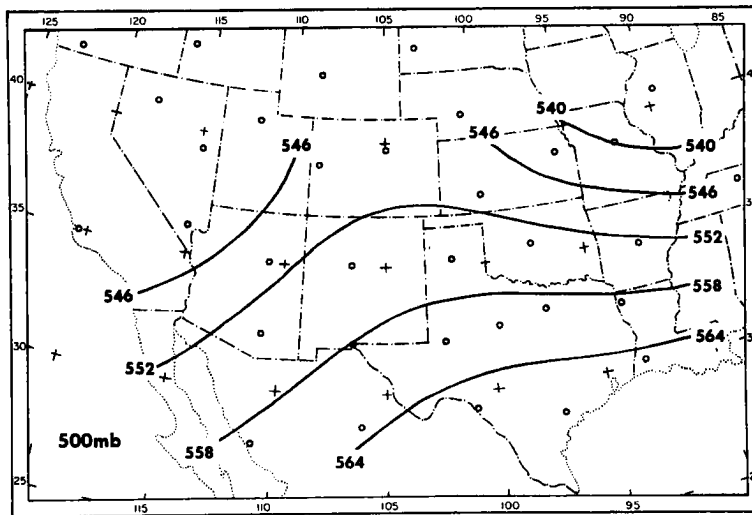
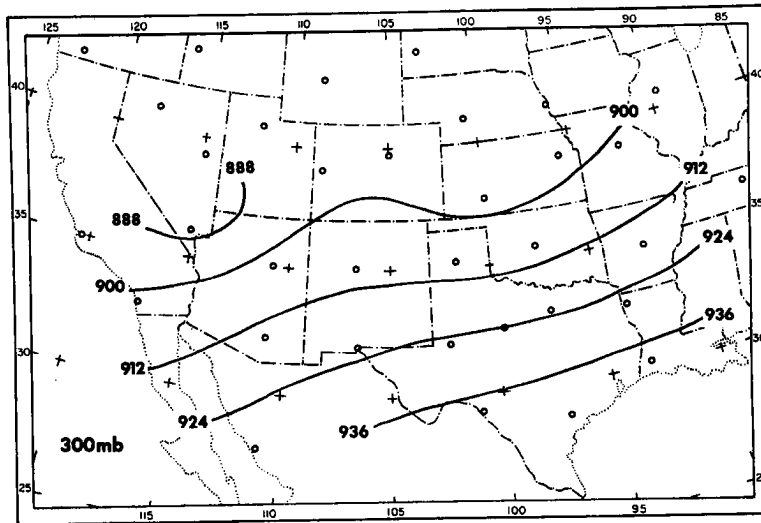


Figure 2.12. Height contours in tens of meters for 1800 GMT March 10, 1969 interpolated 300 mb (above) and 500 mb (below) maps.

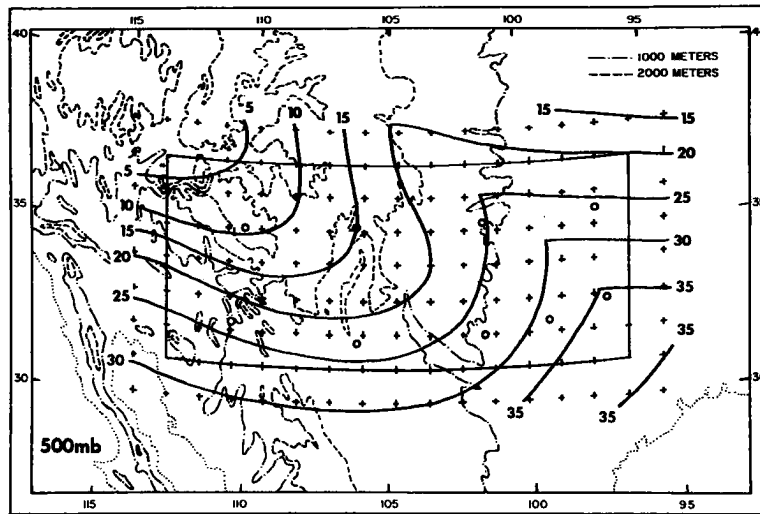
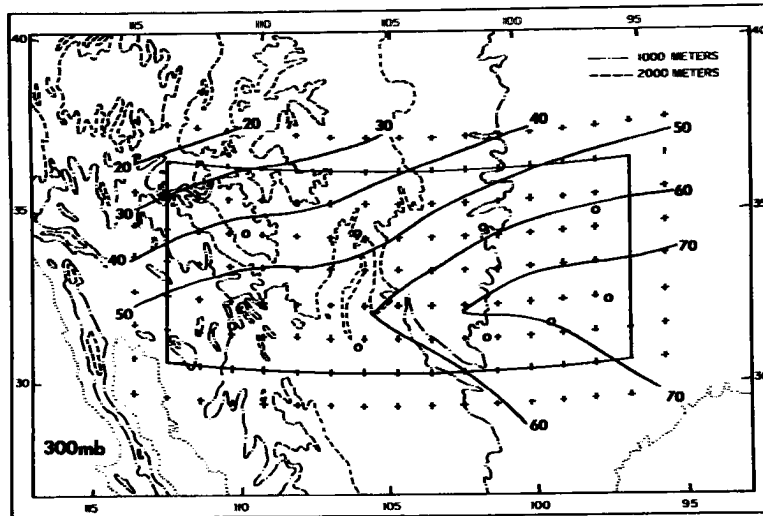


Figure 2.13. Isotachs of zonal wind in meters per second for 1800 GMT March 10, 1969 interpolated 300 mb (above) and 500 mb (below) maps.

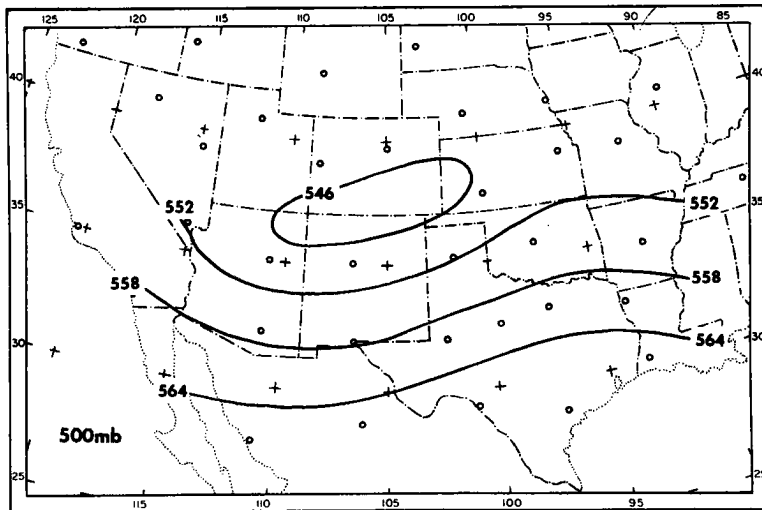
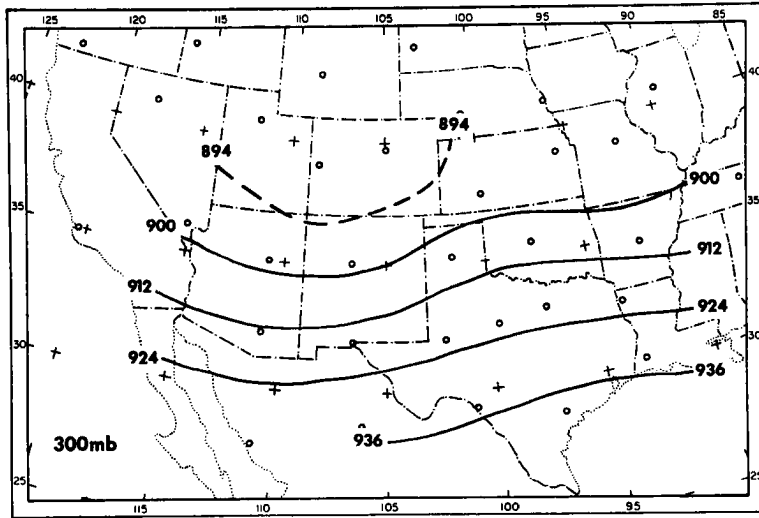


Figure 2.14. Height contours in tens of meters for 1800 GMT March 11, 1969 interpolated 300 mb (above) and 500 mb (below) maps.

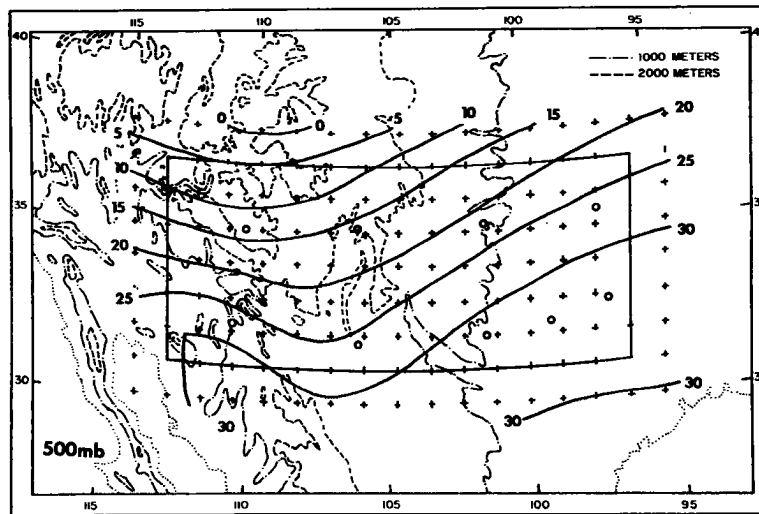
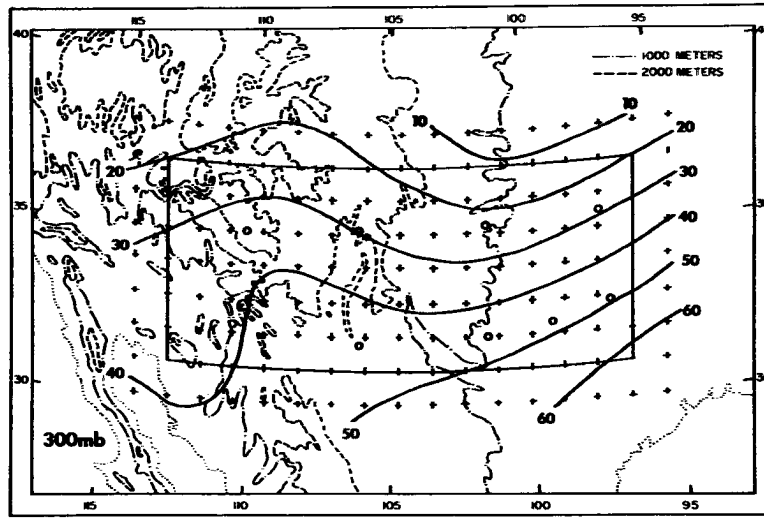


Figure 2.15. Isotachs of zonal wind in meters per second for 1800 GMT March 11, 1969 interpolated 300 mb (above) and 500 mb (below) maps.

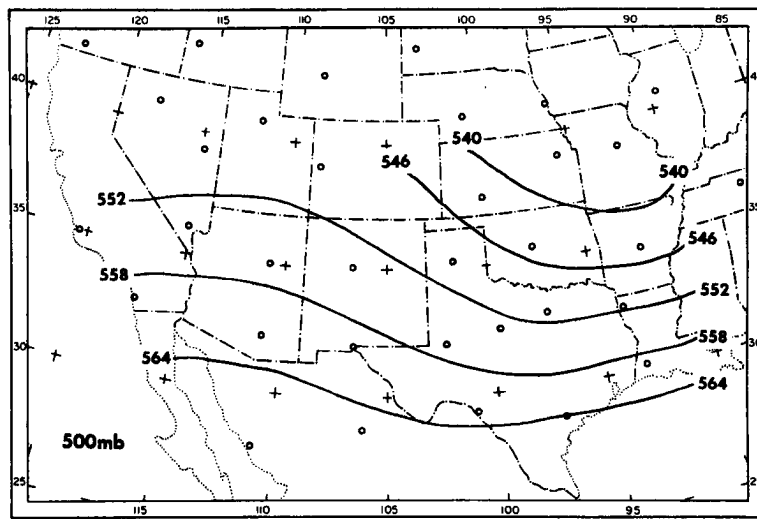
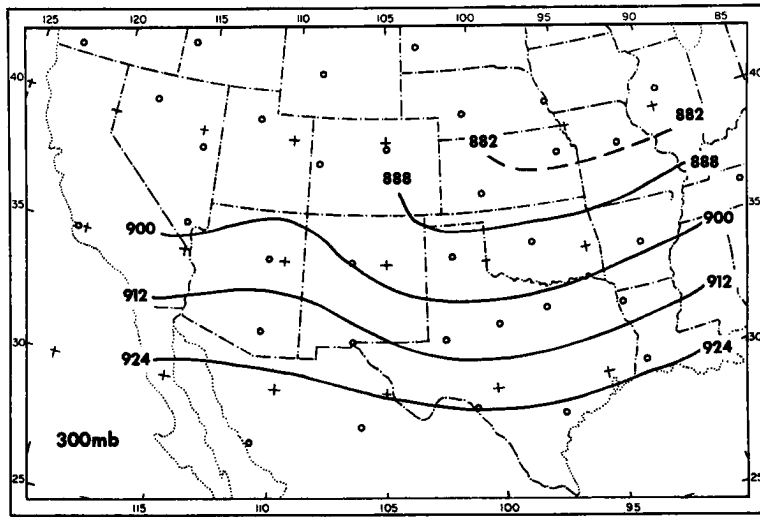


Figure 2.16. Height contours in tens of meters for 1800 GMT March 12, 1969 interpolated 300 mb (above) and 500 mb (below) maps.

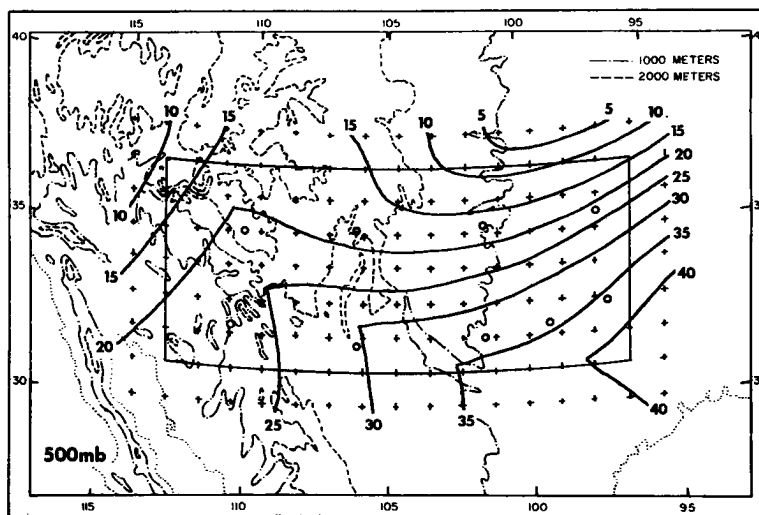
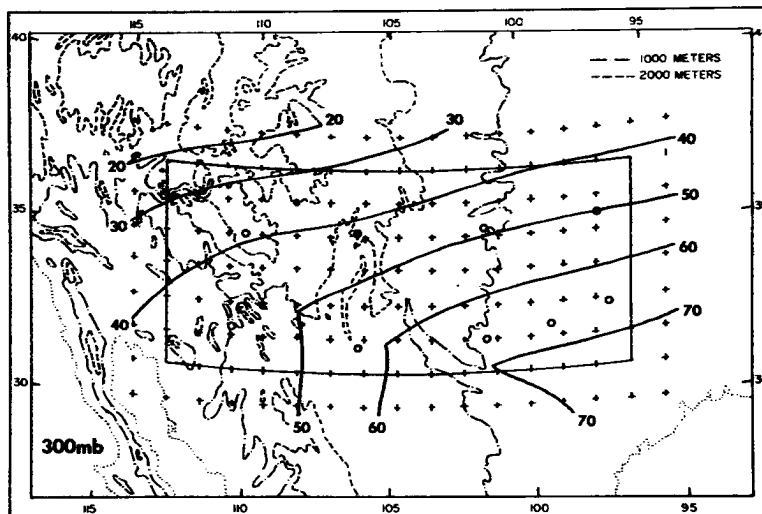


Figure 2.17. Isotachs of zonal wind in meters per second for 1800 GMT March 12, 1969 interpolated 300 mb (above) and 500 mb (below) maps.

### III. ZONAL STRESSES AND ANGULAR MOMENTUM

In the midlatitude belt of westerlies, the absolute angular momentum is often interpreted as an indication of the strength of the circulation. The velocity of the mean westerly motion and the spectral energy of its variance give information on the nature of the general circulation itself (Wooldridge and Reiter, 1970).

Jet streams and jet maxima are intimately related to weather phenomena and influence the upper-level divergence fields associated with midlatitude cyclones (Reiter, 1963). For this reason, the study of the absolute angular momentum fluxes in a preferred region for jet-stream maxima (Lester, 1969) seems particularly appropriate in any study related to the general circulation.

The absolute angular momentum of the atmosphere contains a contribution due to the rotation of the earth itself, called the "omega" angular momentum, and zonal motion of the atmosphere relative to the earth's surface. This momentum can be represented as

$$M = \Omega a^2 \cos^2 \phi + ua \cos \phi \quad (3.1)$$

in which  $M$  is the absolute angular momentum,  $\Omega$  is the angular rotation rate of the earth about its axis,  $a$  is the mean radius of the earth,  $\phi$  is the latitude, and  $u$  is the zonal wind velocity.

The angular momentum of the atmosphere can change through the action of pressure torque and friction torque according to

$$\frac{dM}{dt} = \frac{-r}{\rho} \frac{\partial p}{\partial x} + rF_x \quad (3.2)$$

per unit mass, where  $r = a \cos \phi$ ,  $\rho$  is the atmospheric density,  $\partial p / \partial x$  is the pressure gradient due to differences in zonal pressure across the region of study, and  $F_x$  is the frictional force exerted by shearing stress gradients in the free atmosphere or by frictional "drag" at the earth-atmosphere interface.

A balance equation for absolute angular momentum can be written:

$$\frac{\partial}{\partial t}(\rho M) = -\nabla_3 \cdot \rho M \vec{V}_3 + \rho \frac{dM}{dt} \quad (3.3)$$

per unit volume. Integrating over the volume and making use of Reiter's (1969) averaging notation, the following results:

$$\begin{aligned} \frac{aA}{g} \int_{p_u}^{p_\ell} \left[ \left[ \frac{\Delta u}{\Delta t} \right]_{(\lambda)} \cos \phi \right]_{(\phi)} dp &= - \frac{La}{g} \int_{p_u}^{p_\ell} \left[ c_n (\Omega a \cos^2 \phi + u \cos \phi) \right] dp \\ &\quad (L) \\ &+ \frac{aA}{g} \left[ \omega (\Omega a \cos^2 \phi + u \cos \phi) \right]_{(\phi, \lambda), p_u} \\ &- \frac{aA}{g} \left[ \omega (\Omega a \cos^2 \phi + u \cos \phi) \right]_{(\phi, \lambda), p_\ell} \\ &- aA \int_{p_u}^{p_\ell} \left[ \left[ \frac{\Delta z}{\Delta x} \right]_{(\lambda)} \cos \phi \right]_{(\phi)} dp \\ &+ \frac{aA}{g} \int_{p_u}^{p_\ell} \left[ [F_x]_{(\lambda)} \cos \phi \right]_{(\phi)} dp \end{aligned} \quad (3.4)$$

The left-hand term represents the local change of angular momentum with time; the first term on the right-hand side measures the horizontal convergence; the second and third terms measure the vertical

convergence; the fourth term is due to pressure torque; the last term results from torque exerted by shearing stress gradients.  $A$  is the area of the horizontal upper and lower surfaces of the pressure layer; the subscript  $u$  denotes the upper pressure level; the subscript  $\ell$  indicates the lower pressure level.  $\omega$  has the usual definition  $\omega = dp/dt$ .

Reiter's (1969) symbolism  $[ ]_{(\lambda)}$  indicates an average over longitude,  $[ ]_{(\phi, \lambda), p_i}$  an average over a horizontal surface at a given pressure level,  $[ ]_{(\phi)}$  an average over latitude, and  $[ ]_{(L)}$  an average over the peripheral length.

### Stress Computation

The two-dimensional shearing stress force per unit mass  $\vec{F}_2$  may be expressed (Haurwitz, 1941) as

$$\vec{F}_2 = F_x \vec{i} + F_y \vec{j}, \quad (3.5)$$

where  $\vec{i}$  and  $\vec{j}$  are unit vectors. The stress forces are

$$F_x = \frac{1}{\rho} \frac{\partial \tau_x}{\partial z} = -g \frac{\partial \tau_x}{\partial p} \quad (3.6)$$

and

$$F_y = \frac{1}{\rho} \frac{\partial \tau_y}{\partial z} = -g \frac{\partial \tau_y}{\partial p}, \quad (3.7)$$

in which  $\tau_x$  and  $\tau_y$  are the zonal and meridional stress components, respectively.

The stress force components can be introduced into the equations for horizontal motion, producing for a pressure coordinate system, after dropping second-order terms,

$$F_x = -g \frac{\partial \tau_x}{\partial p} = \frac{du}{dt} - fv + g \frac{\partial z}{\partial x} \quad (3.8)$$

and

$$F_y = -g \frac{\partial \tau_y}{\partial p} = \frac{dv}{dt} + fu + g \frac{\partial z}{\partial y} . \quad (3.9)$$

Alternatively, (3.8) and (3.9) may be written in terms of the ageostrophic wind component (Priestley, 1967)

$$F_x = \frac{du}{dt} - f(v - v_g) \quad (3.10)$$

and

$$F_y = \frac{dv}{dt} + f(u - u_g) . \quad (3.11)$$

If the inertial terms  $du/dt$  and  $dv/dt$  are omitted, as in the special case of uniform unaccelerated flow, (3.10) and (3.11) can be abbreviated to

$$g \frac{\partial \tau_x}{\partial p} = f(v - v_g) \quad (3.12)$$

and

$$g \frac{\partial \tau_y}{\partial p} = -f(u - u_g) , \quad (3.13)$$

as suggested by Sawyer (1958), Priestley (1959), and Reiter (1963). In cases of air flow at or near jet-stream levels, the accelerations and gradients encountered preclude the use of (3.12) and (3.13) and demand the more rigorous treatment of (3.8) and (3.9).

The vertical stress gradients were computed as residuals using (3.8) and (3.9), with the three-dimensional Eulerian form for  $du/dt$  and  $dv/dt$  and assuming  $\omega = 0$  at 75 mb, the top of the volume. Simple center differencing was used for time, using 0000 GMT and 1200 GMT data to obtain  $\partial u/\partial t$  and  $\partial v/\partial t$  at 1800 GMT, and for space differences.

### Zonal Shearing Stresses

Layer values of the zonal shearing stress gradients are presented in vertical profile in Figure 3.1; the units are  $\text{kgm m}^{-1}\text{sec}^{-2}$  per 100 mb pressure thickness or  $10^{-4}$ . The positive mid-profile layers computed for 1800 GMT March 8 underwent a reversal in sign by 1800 GMT March 9, 1969. The change in the profiles of shearing stress gradients followed the formation of an extensive area of mountain waves over New Mexico. A maximum negative gradient occurred near 300 mb on March 9. Following this reversal, the stress gradients remained negative through 1800 GMT March 12, 1969.

The level of maximum wind was used as a zero reference point to construct profiles of stress, with layer increments of the stress gradient summed vertically above and below the LMW. The resulting profiles of zonal shearing stresses (Figure 3.2) emphasize the reversal of sign of the stresses. The arrows indicate the direction of the subgrid-scale vertical flux of zonal momentum through application of the following:

$$\tau_x = - \overline{\rho u'w'} . \quad (3.14)$$

The assumption of no stress at the level of maximum wind does not affect the vertical convergence of zonal momentum due to the stress gradient. Strong vertical convergence at tropopause levels by small-scale processes dominated the profiles from March 9 through March 12; vertical divergence was pronounced at the tropopause on March 8.

The stress gradients computed as residuals from (3.8) and (3.9), the component momentum equations, contain viscous drag forces,

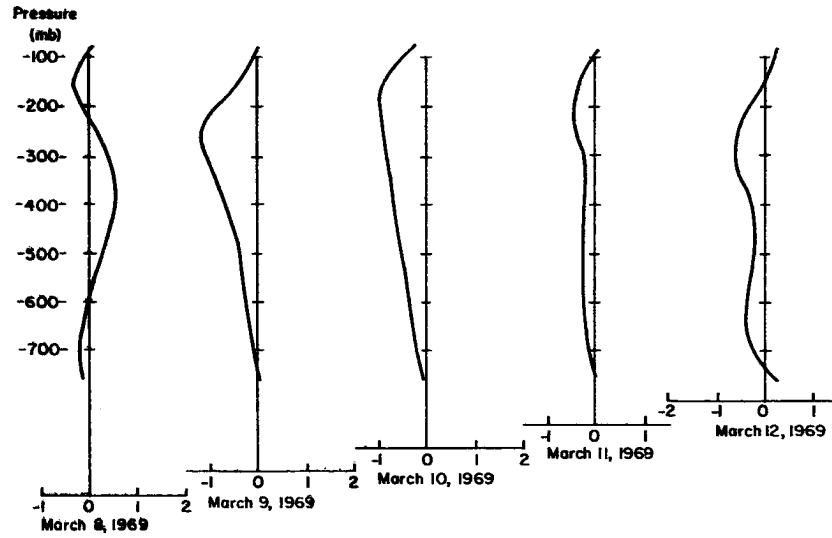


Figure 3.1. Vertical profiles of  $\frac{\delta \tau_x}{\delta p} \Delta p$  in units of  $\text{kgm}^{-1} \text{sec}^{-2}$  per 100 mb, or  $\frac{\delta \tau_x}{\delta \rho}$  in  $10^{-4}$ , at 1800 GMT for days indicated. The pronounced reversal of profile occurred between March 8 and March 9, 1969.

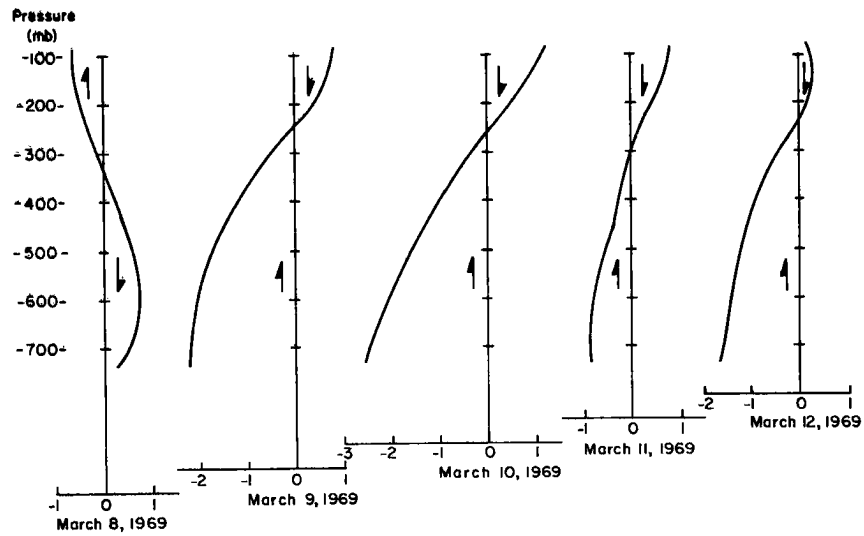


Figure 3.2. Vertical profiles of mean stress ( $\bar{\tau}_x$ ) in units of  $\text{kgm}^{-1} \text{sec}^{-2}$  for 1800 GMT for days indicated. The directions of small-scale fluxes of zonal momentum are indicated by arrows. Multiply by 10 to obtain  $\text{dynes cm}^{-2}$ .

subgrid-scale momentum transport, and computational and data errors. Random data and computational errors were assumed to be acceptably low over the large area of the region.

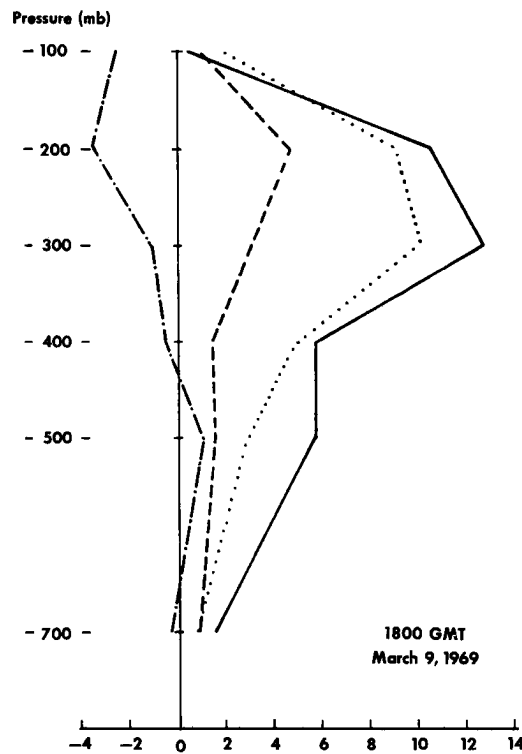


Figure 3.3. Individual terms in the zonal stress gradient computation. The dotted line is the inertial term  $du/dt$ ; dashed line is  $g \frac{\partial z}{\partial x}$ ; dot-dashed line is the Coriolis term  $(-fv)$ ; solid line is  $F_x$ , or  $-g \frac{\partial \tau_x}{\partial p}$ . Units are  $10^{-4} \text{ m sec}^{-2}$  ( $10^{-2} \text{ cm sec}^{-2}$ ).

The individual terms in the zonal stress gradient computation for 1800 GMT March 9 are displayed in Figure 3.3. The pressure-gradient force term ( $g^{\partial z/\partial x}$ ) nearly balanced the Coriolis term ( $-fv$ ); the inertial term  $du/dt$  largely determined the magnitude and sign of  $F_x$ .

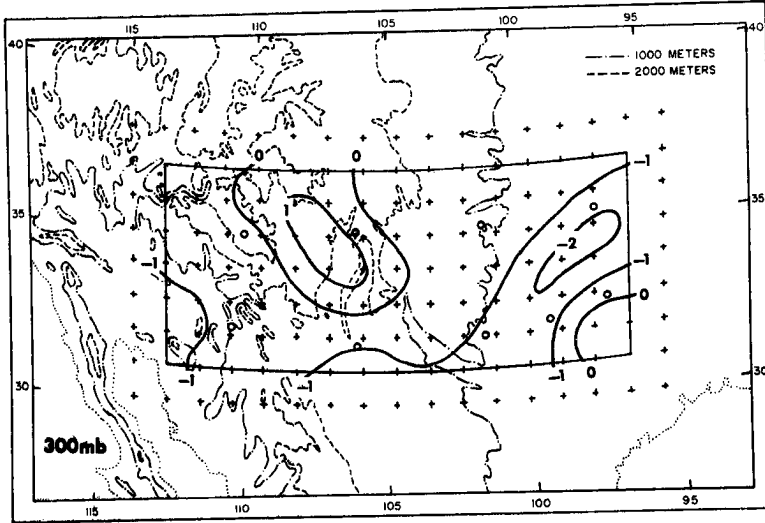
Some bias toward low winds and fair weather could have occurred due to the rapid displacement of rawinsondes in high winds and to short pilot balloon runs in cloudy areas (Reiter, 1963). Subjective and objective analysis techniques would tend to smooth data and reduce the gradients; these factors would serve to reduce the residual stress values somewhat.

The viscous drag force can be estimated through application of the expression

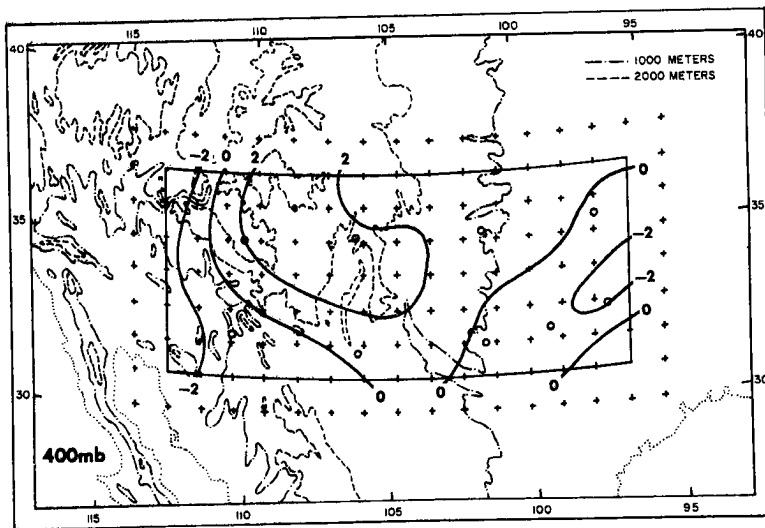
$$D = \vec{V}_2 \cdot \vec{F}_2, \text{ where} \quad (3.15)$$

$D$  is the viscous dissipation. If the viscous dissipation in  $50 \text{ m sec}^{-1}$  flow amounts to one watt  $\text{m}^{-2}$  in a layer 200 mb thick, the stress gradient totals  $0.2 \text{ dynes cm}^{-2}$ . This is two orders of magnitude smaller than the zonal stress gradients shown in Figure 3.1 over a 200 mb layer at the tropopause on March 9 and 10, 1969.

Contours of zonal stresses on isobaric surfaces shown in Figures 3.4(a)-(d) and 3.5(a)-(d) exhibit the change of direction of the vertical flux of zonal momentum on the subgrid scales that took place between 1800 GMT March 8 and 1800 GMT March 9, 1969. The strongest downward transport on March 8 appeared over eastern New Mexico and western Texas near  $35\text{N } 104\text{W}$  at the lowest levels. The greatest upward

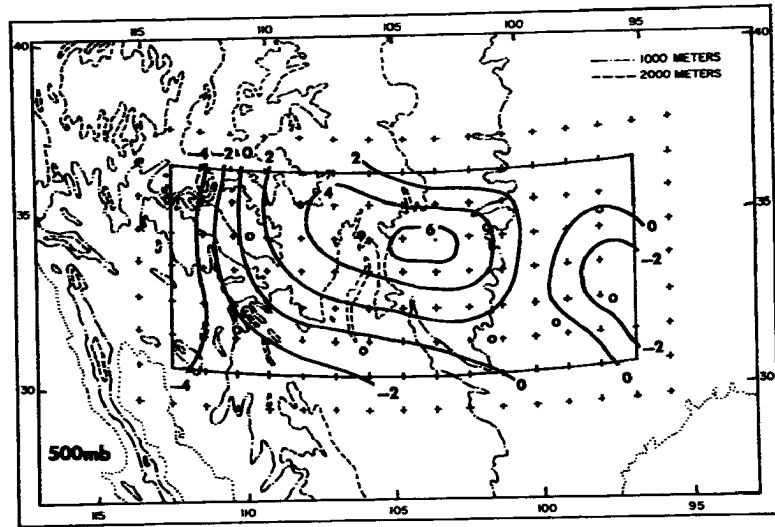


(a)

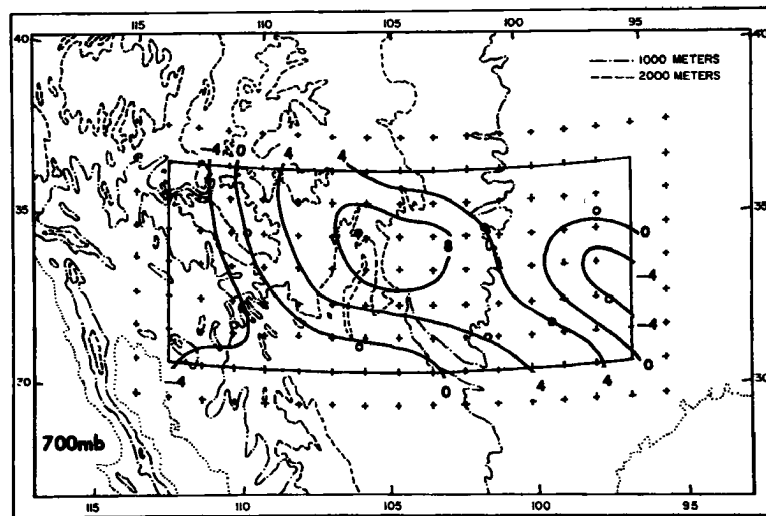


(b)

Figures 3.4(a) and (b). Contours of zonal stress ( $\tau_x$ ) for 1800 GMT March 8, 1969 at the 300 mb and 400 mb levels. Units are  $\text{kgm m}^{-1} \text{sec}^{-2}$ . Multiply by 10 to obtain  $\text{dynes cm}^{-2}$ .

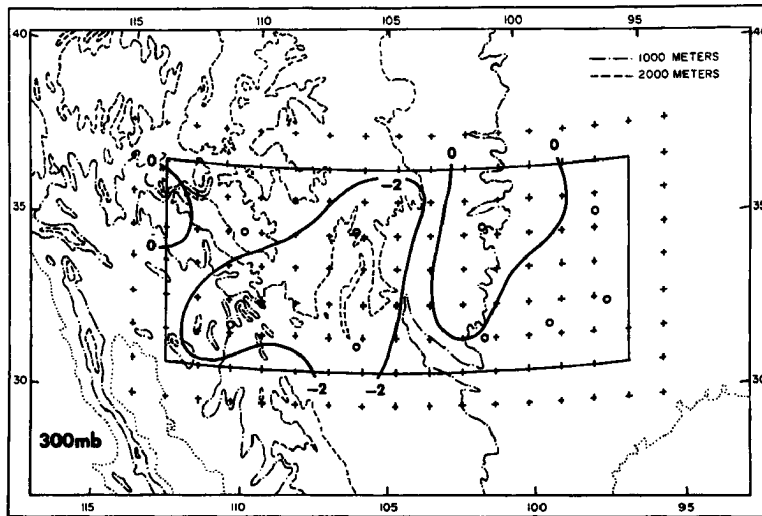


(c)

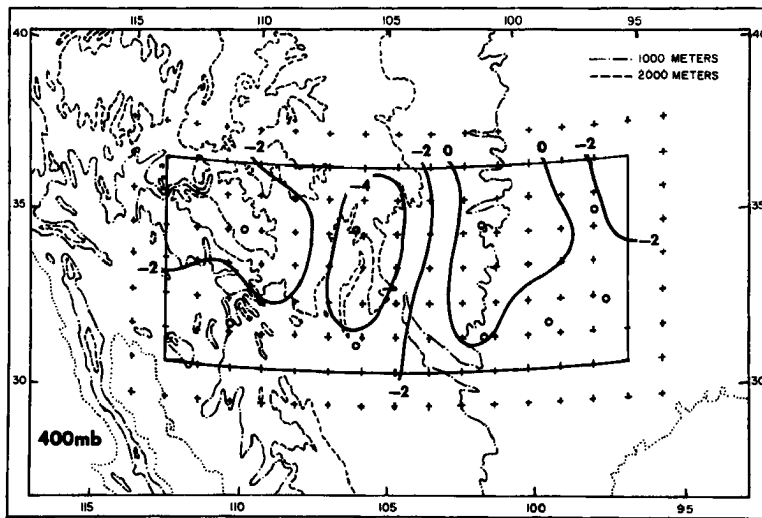


(d)

Figures 3.4(c) and (d). Same as Figures 3.4(a) and (b) except for 500 mb and 700 mb.

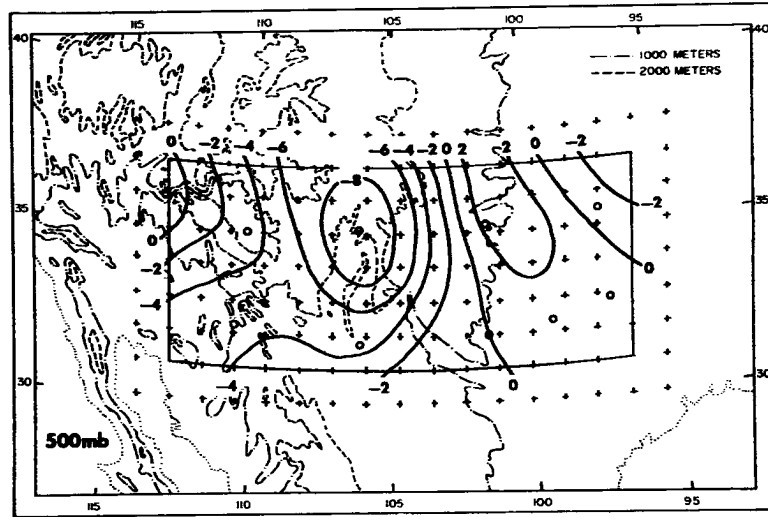


(a)

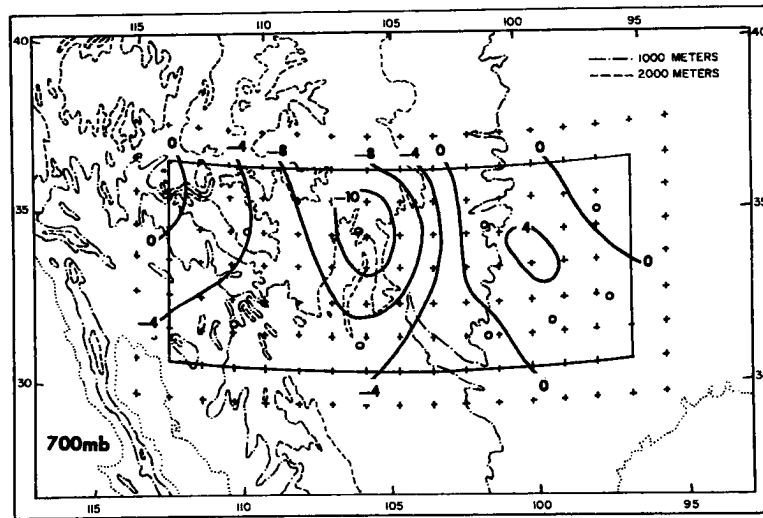


(b)

Figures 3.5(a) and (b). Contours of zonal stress ( $\tau_x$ ) for 1800 GMT March 9, 1969 at the 300 mb and 400 mb levels. Units are  $\text{kgm m}^{-1} \text{sec}^{-2}$ . Multiply by 10 to obtain  $\text{dynes cm}^{-2}$ .



(c)



(d)

Figures 3.5(c) and (d). Same as Figures 3.5(a) and (b) except for 500 mb and 700 mb.

Table 3.1. Summary of angular momentum terms. Units for the individual levels are  $10^3 \text{ m}^2 \text{ sec}^{-2}$  ( $10^7 \text{ cm}^2 \text{ sec}^{-2}$ ); units for the totals (integrated over pressure) are  $10^6 \text{ kgm sec}^{-2}$  ( $10^9 \text{ gm sec}^{-2}$ ).

Level (mb)	Local change (computed)	Horizontal convergence	Vertical convergence	Pressure torque	Stress torque	Residual (local change)	Im-balance
1800 GMT March 1969							
100	0.52	0.48	-0.27	-0.71	0.65	0.15	0.19
150	0.00	1.20	-0.88	-1.30	1.80	0.82	0.82
200	0.18	-1.10	0.69	0.05	0.62	0.26	0.08
300	0.21	-1.20	1.70	0.57	-1.10	-0.03	-0.24
400	0.33	-1.00	1.10	0.98	-1.20	-0.12	-0.45
500	0.06	-0.40	0.10	0.81	-0.53	-0.02	-0.08
700	0.18	-0.23	-0.35	0.37	0.33	0.12	-0.06
TOTAL	1.30	-3.20	2.30	2.40	-0.81	0.69	-0.61
1800 GMT March 9, 1969							
100	0.19	-1.40	1.70	-0.54	0.34	0.10	-0.09
150	0.13	-3.10	3.40	-1.50	0.98	-0.28	-0.41
200	1.30	-2.90	1.92	-2.10	3.40	0.32	-0.98
300	1.10	-3.60	0.24	-1.40	6.20	1.40	0.30
400	0.42	-2.00	-0.43	-0.70	3.40	0.27	-0.15
500	0.04	-0.65	-1.10	-0.71	2.60	0.16	0.12
700	0.38	-0.15	-0.23	-0.33	0.65	-0.06	-0.44
TOTAL	3.50	-11.30	1.70	-6.40	17.90	1.90	-1.60
1800 GMT March 10, 1969							
100	-0.46	-1.00	1.40	-1.10	1.00	0.30	0.76
150	0.44	-2.20	2.50	-2.00	2.10	0.40	-0.04
200	0.30	-2.10	2.20	-2.20	1.80	-0.30	-0.60
300	-0.18	-1.60	0.62	-2.40	3.50	0.12	0.30
400	0.53	-0.71	0.02	-2.00	3.40	0.71	0.18
500	0.29	-0.08	-0.44	-1.40	2.30	0.38	0.09
700	0.03	0.17	-0.67	-0.88	1.40	0.02	0.01
TOTAL	1.10	-5.30	2.10	-11.20	15.70	1.30	0.20

Table 3.1. Continued.

Level (mb)	Local change (computed)	Horizontal convergence	Vertical convergence	Pressure torque	Stress torque	Residual (local change)	Imbalance
1800 GMT March 11, 1969							
100	-0.08	-0.56	0.77	-0.94	0.40	-0.33	-0.25
150	-0.48	-1.20	1.40	-1.80	1.50	-0.10	0.38
200	-0.87	-3.00	2.40	-1.80	1.90	-0.50	0.37
300	-1.00	-1.30	0.94	-1.20	0.90	-0.66	0.34
400	0.31	-1.20	0.44	-0.83	1.50	-0.09	-0.39
500	-0.01	-0.63	-0.56	-0.34	1.40	-0.13	-0.12
700	0.34	-0.04	-0.50	0.30	0.45	0.21	-0.13
TOTAL	-1.10	-6.70	2.60	-4.80	7.60	-1.00	-0.20
1800 GMT March 12, 1969							
100	-1.00	-0.77	-0.87	-0.65	1.00	-1.30	-0.30
150	0.42	-0.83	-0.15	-0.38	0.84	-0.52	-0.94
200	-0.33	-1.10	-0.06	0.03	0.78	-0.35	-0.02
300	-0.37	-4.00	-0.16	1.20	3.10	0.14	0.51
400	-0.78	-2.80	-0.24	0.82	1.20	-1.00	-0.22
500	0.38	-2.60	0.54	1.20	1.00	0.14	-0.24
700	0.09	-1.20	-0.03	0.57	0.90	0.24	0.15
TOTAL	-0.96	-14.60	-0.29	4.30	9.00	-1.60	-0.64

transport took place over the rugged terrain of central and east-central New Mexico, again at 775 mb, on March 9. One mountain peak northeast of Albuquerque rises over 4 km, and several peaks and ridges south of the city extend upward in excess of 3 km.

#### Angular Momentum Budgets

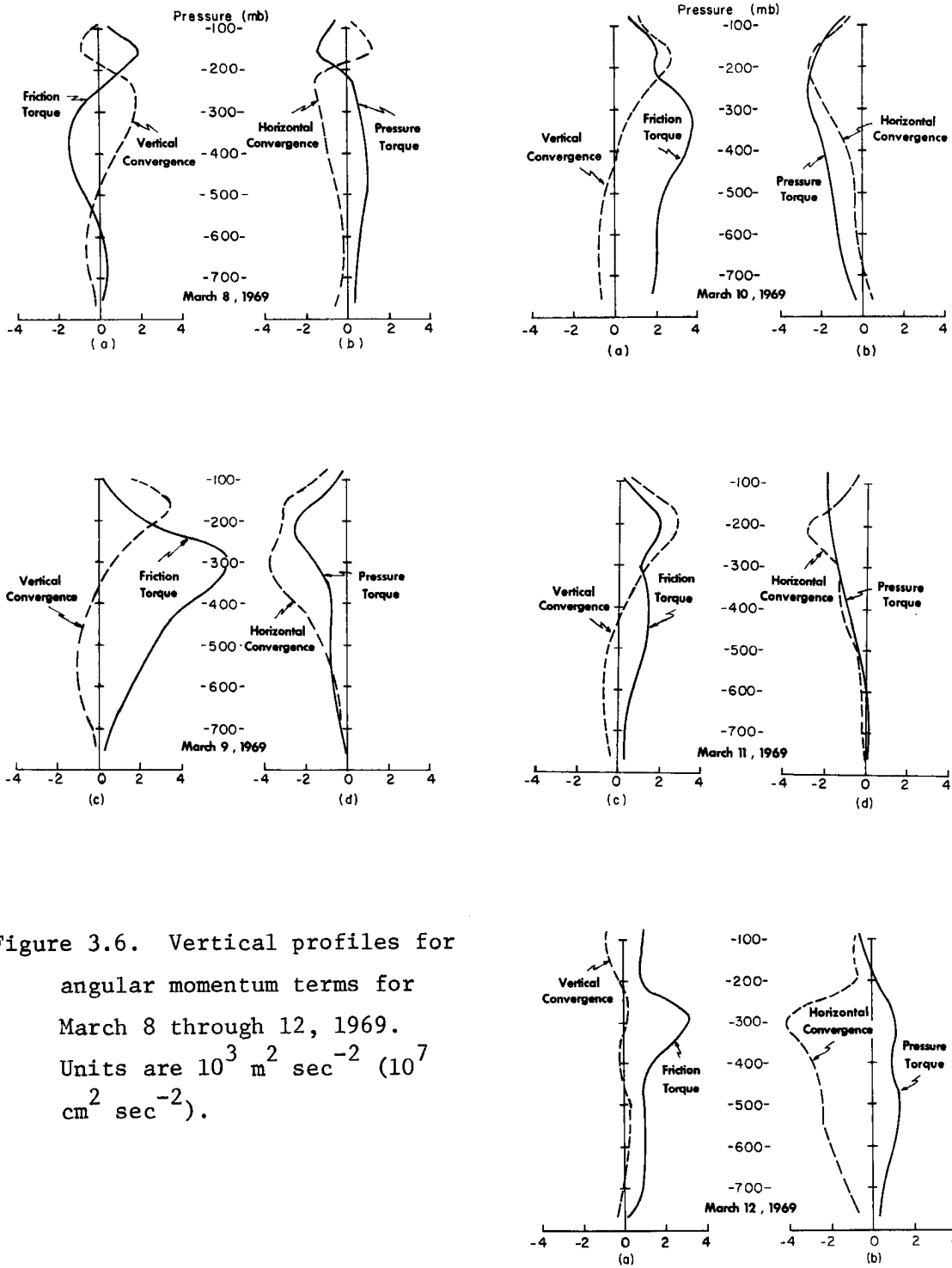
The magnitudes and signs of the stress gradients suggested the working of a vigorous physical process which acted to move zonal momentum upward against the momentum gradient. This counter-gradient flux implies a vertical wave propagation with a downstream tilt of the vertical axis with height. Three checks were instituted to verify the nature of the stresses: an absolute angular momentum budget, a vorticity budget, and a separate calculation of the stress gradient in an isentropic coordinate system.

The angular momentum terms listed in Table 3.1 bring out the change in character of the momentum fluxes which occurred between March 8 and March 9. The stress torque, negative in sign and small in magnitude at 1800 GMT March 8, became positive by 1800 GMT March 9 and dominated the momentum budget, together with the pressure torque and horizontal convergence. The stress torque remained positive, but diminished, through 1800 GMT March 12. From March 9 through March 12, the stress torques and pressure torques remained large and opposite in sign. The pressure torques changed signs on March 9, became large in magnitude and negative on March 10, then positive again on March 11 and 12, 1969.

Except for March 8, the total stress torque, indicating the vertical flux of relative angular momentum on small scales, maintained

values about one order of magnitude larger than the sum of the layer vertical convergences due to large-scale motions. The local change of angular momentum reflected the general increase in zonal flow intensity between March 8 and March 10, and a decrease following March 10, 1969. The computed local change (first column) differed from the residual "local change" by the amount shown in the "imbalance" column in Table 3.1. Balance over the volume was largely struck between horizontal convergence, pressure torque, and stress torque for the period.

The main terms of the angular momentum budgets are presented in vertical profile in Figure 3.6. The vertical convergence includes transport by the mean flow and by synoptic-scale eddies. The profiles have been constrained pass through computed mean values for each layer beginning with 700 mb and ending at 100 mb.



#### IV. VORTICITY BUDGETS

The stress values exhibited in vertical profile in Figure 3.2 were based on computations utilizing interpolated pressure heights and wind components. The dependence on these parameters in the pressure-coordinate system suggested a requirement for a separate check on the accuracy of the interpolated data. To this purpose, a vorticity balance equation was applied to the 1800 GMT data for the March 8 and March 9 cases. On March 8 the sign of the shearing stress indicated a vertical flux downward from the level of maximum wind; the contra-directional flux on March 9 was tested through the balance of the vorticity budget with twisting and stress terms included.

The vorticity balance equation is derived from the equations of motion in pressure coordinates

$$\frac{\partial u}{\partial t} + \vec{V}_3 \cdot \nabla_3 u = -g \frac{\partial z}{\partial x} + fv + F_x \quad (4.1)$$

and

$$\frac{\partial v}{\partial t} + \vec{V}_3 \cdot \nabla_3 v = -g \frac{\partial z}{\partial y} - fu + F_y \quad (4.2)$$

The computational form, using Reiter's (1969) notation becomes

$$\begin{aligned} \frac{A}{g} \int_{p_u}^{p_\ell} \left[ \frac{\partial \zeta}{\partial t} \right]_{(\phi, \lambda)} dp &= - \frac{L}{g} \int_{p_u}^{p_\ell} [(\zeta + f)c_n]_{(L)} dp + \\ &+ \frac{A}{g} \left\{ [\omega(\zeta + f)]_{(\phi, \lambda), p_u} - [\omega(\zeta + f)]_{(\phi, \lambda), p_\ell} \right\} + \\ &+ \frac{A}{g} \int_{p_u}^{p_\ell} \left[ \frac{\partial \omega}{\partial y} \frac{\partial u}{\partial p} - \frac{\partial \omega}{\partial x} \frac{\partial v}{\partial p} \right]_{(\phi, \lambda)} dp + \\ &+ \frac{A}{g} \int_{p_u}^{p_\ell} \left[ \frac{\partial F_y}{\partial x} - \frac{\partial F_x}{\partial y} \right]_{(\phi, \lambda)} dp . \end{aligned} \quad (4.3)$$

$\zeta$  in (4.3) is the relative vorticity about a vertical axis;  $c_n$  is the velocity normal to the bounding surface, positive outward. The mathematical symbolism  $[ ]_{(\phi, \lambda)}$  indicates an area mean;  $[ ]_{(L)}$  indicates an average around the perimeter. Subscripts without parentheses retain their usual meaning. The left-hand side measures the local change of vorticity; the first term on the right-hand side is the horizontal convergence of absolute vorticity; the second term on the right-hand side gives the vertical convergence of absolute vorticity; the third term represents conversion of vorticity about a horizontal axis to a contribution about the vertical axis (the "twisting term"); the last term indicates the contribution to vorticity through the action of shearing stresses. Centered differencing was applied to time and space.

Table 4.1 contains the elements of the absolute vorticity balance equation for 1800 GMT March 8 and 1800 GMT March 9, 1969. The sum of the four terms on the right-hand side of (4.3) is expressed as a residual (local change); the difference between the residual and the computed local change constitutes the imbalance listed in the last column in the table. Although the imbalance of individual layers was on the same order as other terms in the same layer, it was an order of magnitude smaller than the twisting or stress terms when integrated vertically over pressure.

The stress term for 1800 GMT March 8 exceeded the sum of the vertical convergence and the twisting terms for the volume; on March 9 the stress term reversed its sign, as did the convergence and twisting terms. The magnitude of all terms indicated that none of them could be systematically excluded in the computation without resulting in a considerable error in the vorticity balance.

Table 4.1. Summary of vorticity terms. Units for the individual levels are  $10^{-9} \text{ sec}^{-2}$ ; units for the totals (integrated over pressure) are  $10^{-6} \text{ sec}^{-2}$ .

Level (mb)	Local change (computed)	Horizontal convergence	Vertical convergence	Twisting term	Stress term	Residual (local change)	Imbalance
1800 GMT March 8, 1969							
100	-0.33	-0.88	0.31	0.00	0.24	-0.11	0.22
150	-0.19	0.48	0.27	-0.29	0.10	0.56	0.75
200	0.14	0.92	0.40	-0.54	-0.41	0.37	0.23
300	0.33	-0.67	0.61	0.27	-0.18	0.03	-0.30
400	-0.26	-0.22	0.61	0.50	-1.42	-0.53	-0.27
500	-0.49	0.00	0.30	0.41	-1.41	-0.70	-0.21
700	-0.02	-0.10	0.80	0.18	-0.21	-0.05	-0.03
TOTAL	-0.85	-0.63	2.40	1.10	-4.00	-1.00	-0.15
1800 GMT March 9, 1969							
100	-0.65	0.31	-0.88	0.34	-0.15	-0.38	0.27
150	-0.79	0.50	-0.56	-0.10	-0.29	-0.45	0.34
200	-0.81	-0.17	-0.38	-0.36	0.28	-0.63	0.18
300	-0.83	-1.37	-0.40	-0.30	1.52	-0.55	0.28
400	-0.70	-0.89	0.27	-1.06	0.88	-0.80	-0.10
500	-0.64	-0.33	1.21	-1.54	0.20	-0.46	0.18
700	-0.62	-0.09	-0.51	-0.36	0.21	-0.75	-0.13
TOTAL	-4.90	-2.60	-0.22	-4.40	3.10	-4.10	0.80

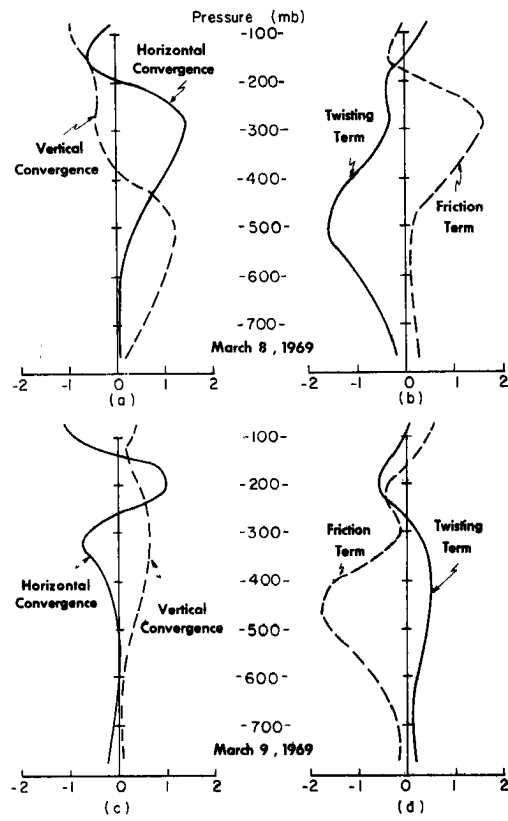


Figure 4.1. Vertical profiles for vorticity budgets for March 8 and 9, 1969. Units are  $10^4 \text{ kgm sec}^{-2}$  per mb, or  $10^{-9} \text{ sec}^{-2}$ .

The twisting term exhibited maxima at mid-level and minima at upper levels; stress values were greatest at 500 mb at 1800 GMT March 8 and at 300 mb at 1800 GMT March 9, 1969. Horizontal fluxes showed maxima near the level of maximum winds while vertical convergences were maximized at 300 to 400 mb on March 8, and at 500 mb on March 9.

The vertical profiles of the vorticity budget terms (Figure 4.1) indicate the change of the sign and location of these maxima in unit pressure thicknesses. The reversal in sign of the stress term appears in the profiles for March 8 and 9. The imbalance of terms for the separate layers indicates that a requirement existed for vertical redistribution of vorticity by subgrid-scale motions. The balance of the vorticity terms substantiates the magnitude and direction of the shearing stresses presented in Chapter III.

## V. KINETIC ENERGY GENERATION AND DISSIPATION

The large shearing stresses, equated to vertical momentum fluxes in Chapter III, suggest a considerable small-scale activity of the same order of magnitude as the synoptic scale motions. These cases, then, present an opportunity to investigate the efficacy of the application of energy equations such as those used by Kung (1966, 1969) to all scales of motion.

The direct calculation of frictional dissipation as a scalar product of velocity and frictional force could not be accomplished at any one instant of time due to the apparent vertical flux by gravity waves. Consequently, dissipation was computed as a residual in the kinetic energy budget in the form:

$$\begin{aligned}
 -D = & -\frac{A}{g} \int_{p_u}^{p_\ell} \left[ \frac{\partial K}{\partial t} \right]_{(\phi, \lambda)} dp - \frac{L}{g} \int_{p_u}^{p_\ell} [Kc_n]_{(L)} dp + \\
 & + \frac{A}{g} \{ [K\omega]_{(\phi, \lambda), p_u} - [K\omega]_{(\phi, \lambda), p_\ell} \} \\
 & - A \int_{p_u}^{p_\ell} [\vec{V}_2 \cdot z]_{(\phi, \lambda)} dp .
 \end{aligned} \tag{5.1}$$

Reiter's (1969) mathematical symbolism has again been used in (5.1) to indicate the computational procedure. The first term on the right-hand side represents the local change of kinetic energy with time; the second, the horizontal convergence; the third, the vertical convergence between pressure surfaces; the last term, the generation of kinetic energy within the volume.  $D$  is the dissipation;  $K$  is the horizontal kinetic energy,  $(u^2 + v^2)$ , per unit mass.

### Kinetic Energy Computational Results

The results of applying the pressure-coordinate kinetic energy budget to the volume are related in Table 5.1 for 1800 GMT March 8-12, 1969. The local change (first column) is directly calculated; the dissipation (last column) is the residual of all the other columns. The estimated error interval for each term has been appended to the total for each day. The vertical profiles of the kinetic energy terms in Figure 5.1 exhibit the relative importance of the individual terms.

The vertical profiles of the mean zonal wind shown in Figure 5.2 reflect the local changes characterized in Table 5.1. The large local change increase indicated in the table at 300 and 400 mb at 1800 GMT March 8 agrees with the changing profile resulting in sharply increased mean winds found on March 9 at upper levels. Decreasing local changes centered at 300 mb on March 10 and 11 indicate the reduction in zonal flow found in the profiles on March 11 and 12, 1969.

Except for March 10, a net outflow of kinetic energy occurred through the vertical boundaries of the volume. This largely resulted from downstream outflow at considerably higher velocity than the upstream inflow (see Figure 5.2). The vertical convergence term included only synoptic-scale eddies and mean vertical mass flux; no analogy existed in the set of terms in (5.1) for subgrid fluxes as compared to the shearing stress term in the momentum equations (3.8 and 3.9). Subgrid-scale energy sources and sinks also were excluded in the equations.

Generation on March 8 proved extremely large when compared to long term means (Kung, 1967), occurring through a deep layer from

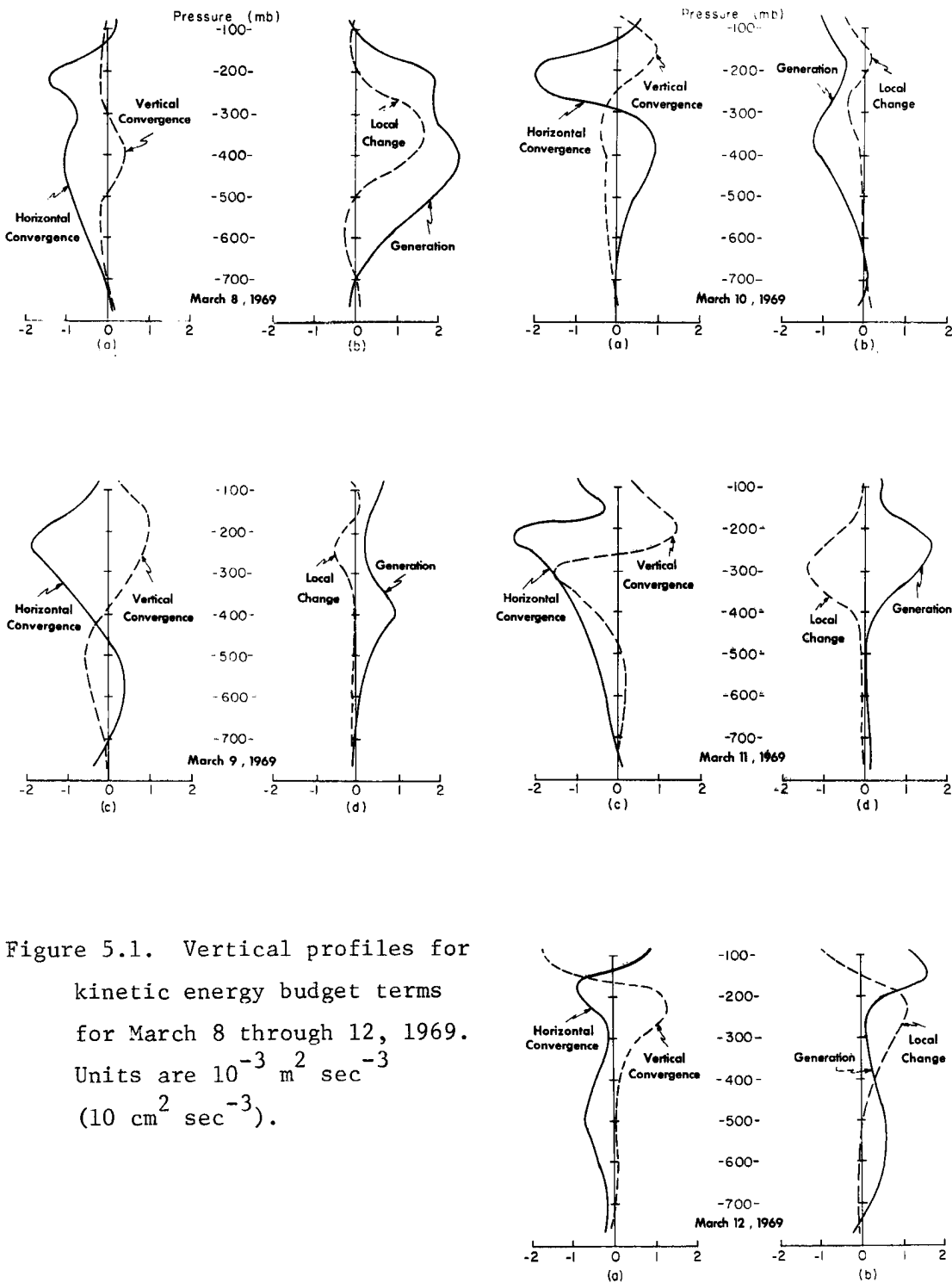
Table 5.1. Summary of kinetic energy terms. Units for the individual levels are  $10^{-3} \text{ m}^2\text{sec}^{-3}$  ( $10 \text{ cm}^2\text{sec}^{-3}$ ); units for the totals (integrated over pressure) are  $\text{watts m}^{-2}$ .

Level (mb)	Local change	Horizontal convergence	Vertical convergence	Generation	Dissipation
1800 GMT March 8, 1969					
100	-0.9	1.9	-0.5	-0.2	2.2
150	-0.4	-1.6	-1.0	4.7	2.5
200	0.8	-12.6	-1.9	17.3	2.0
300	7.0	-7.4	-0.5	18.0	3.1
400	6.6	-9.9	4.2	23.5	11.2
500	-0.4	-8.3	-0.9	12.2	3.4
700	-0.1	-1.6	-0.2	0.2	-1.5
TOTAL	12.9±1.3*	-41.9±5.9*	-0.1±0.02*	75.4±6.8*	20.5±14.0*
1800 GMT March 9, 1969					
100	0.9	-3.4	3.6	6.3	5.6
150	1.1	-9.3	8.4	3.3	1.3
200	-3.5	-15.4	7.6	2.9	-1.4
300	-2.1	-12.4	6.3	3.0	-1.0
400	0.0	-3.9	-1.5	8.9	3.5
500	-0.6	2.0	-5.3	2.8	0.1
700	-0.8	0.1	-1.4	-0.4	-0.8
TOTAL	-6.0±0.6	-30.7±4.3	6.1±1.1	22.4±2.0	3.9±8.0
1800 GMT March 10, 1969					
100	-3.0	4.4	4.5	-9.1	2.8
150	0.5	-4.7	9.2	-6.0	-2.0
200	0.3	-18.3	5.4	-4.7	-17.9
300	-2.9	2.1	-3.1	-9.2	-7.3
400	-1.4	9.2	-2.9	-10.3	-2.6
500	-0.2	4.0	-3.0	-5.5	-4.3
700	0.4	0.8	-0.7	0.9	0.6
TOTAL	-5.2±0.5	4.8±0.7	-0.8±0.2	-37.3±3.4	-28.0±4.8

Table 5.1. Continued

Level (mb)	Local change	Horizontal convergence	Vertical convergence	Generation	Dissipation
1800 GMT March 11, 1969					
100	-0.8	-8.0	4.2	4.2	1.2
150	-1.8	-2.6	9.2	3.9	12.3
200	-5.2	-24.4	13.7	13.7	8.2
300	-13.3	-13.5	-15.4	12.4	-3.2
400	-2.7	-10.3	-4.2	2.5	-9.3
500	-1.0	-2.2	1.7	0.1	0.6
700	-0.5	-0.5	0.7	1.6	2.3
TOTAL	-23.5±2.4	-51.8±7.2	1.2±0.2	32.2±2.9	5.3±10.7
1800 GMT March 12, 1969					
100	-7.3	7.4	-15.1	13.1	12.7
150	1.6	-6.0	-6.7	15.0	0.7
200	9.5	-7.3	12.0	3.9	-0.9
300	7.0	-1.2	5.6	1.1	-1.5
400	3.1	-3.7	2.2	3.3	-1.3
500	0.4	-6.4	0.8	5.8	-0.2
700	-0.5	-1.4	-0.3	1.6	0.4
TOTAL	14.0±1.4	-21.7±3.0	6.6±1.1	32.9±3.0	3.7±8.5

\*For an explanation of the error analysis, see Appendix A.



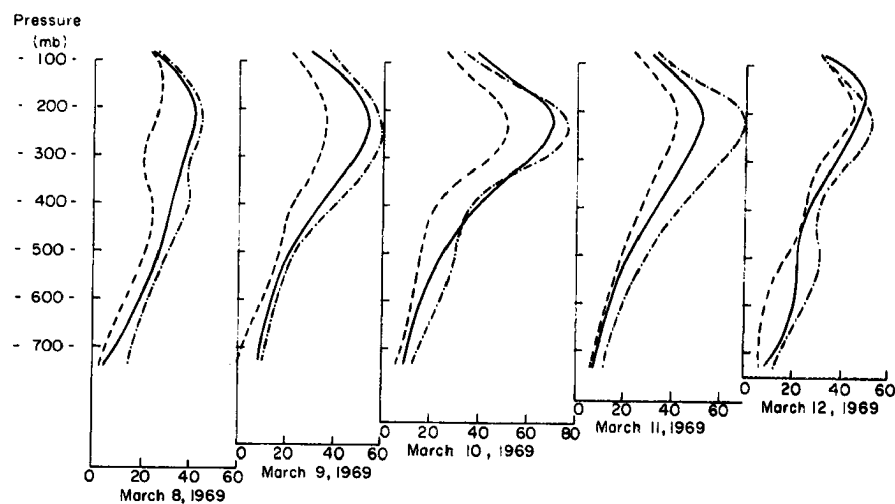
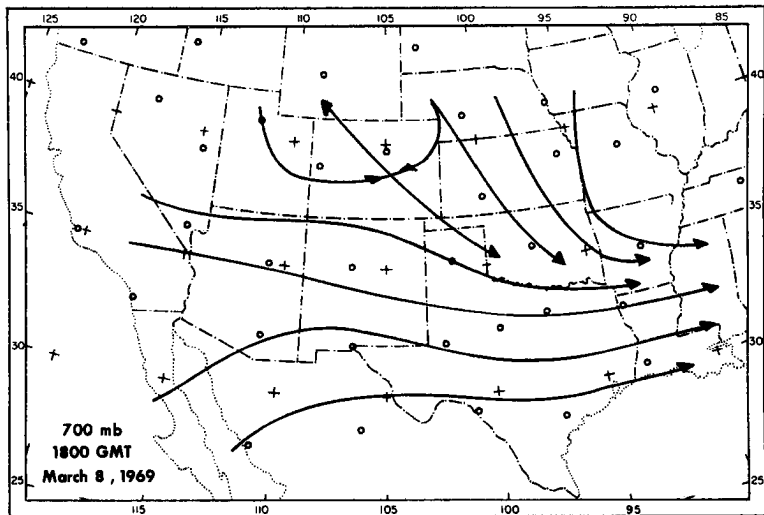
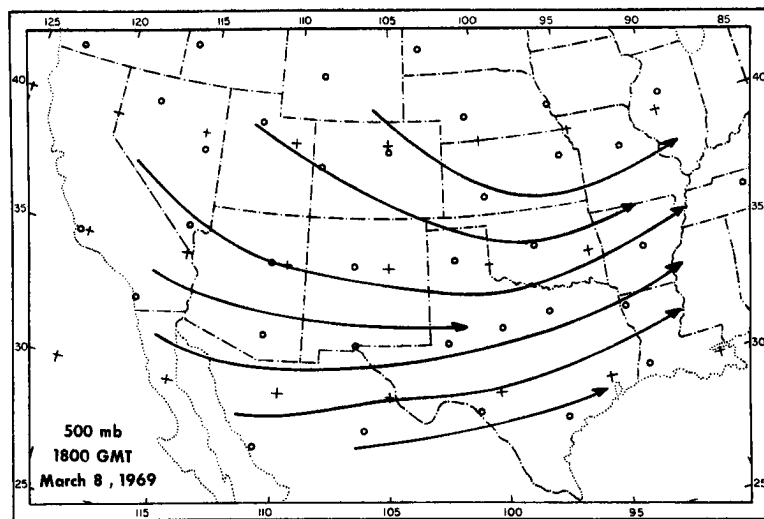


Figure 5.2. Vertical profiles of the mean zonal wind velocity for the region of study in meters sec<sup>-1</sup>. The solid line is for the entire region; the dashed line is for the western boundary; the dot-dashed line is for the eastern boundary.

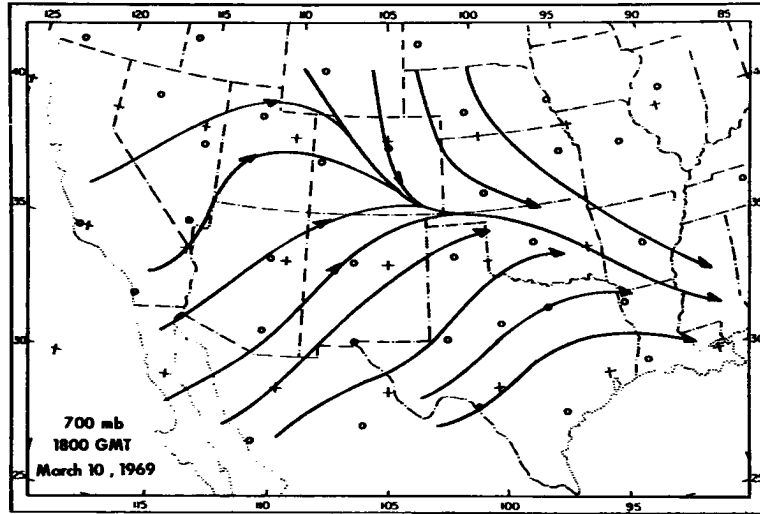


(a)

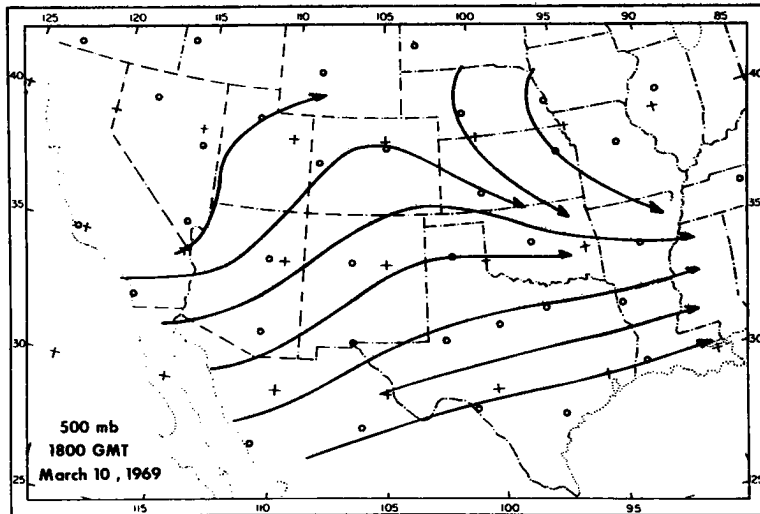


(b)

Figures 5.3(a) and (b). Streamline analysis for 700 mb (a) and 500 mb (b) for 1800 GMT March 8, 1969.



(a)



(b)

Figures 5.4(a) and (b). Streamline analysis for 700 mb (a) and 500 mb (b) for 1800 GMT March 10, 1969.

175 to 600 mb. The generation rate diminished by 1800 GMT March 9, with a maximum again at 400 mb, becoming negative except for the lowest layer by 1800 GMT March 10. The level of maximum generation occurred at 200 mb on March 11 and at 150 mb and 500 mb on March 12.

The level of maximum horizontal divergence was by no measure uniformly located, as shown in the second column. A maximum was found at 500 mb on March 8, 300 mb on March 9, 200 mb on March 10 and 11, and again at 500 mb on March 12. Only on March 10 did appreciable influx through vertical boundaries take place. Figures 5.3(a) and (b) and 5.4(a) and (b) illustrate the backing of the wind along the southern boundary of the computational region between March 8 and March 10. At 700 mb this caused a line of convergence along the northern edge of the region on March 10; at 500 mb the convergence was confined to the northeastern portion, over Oklahoma and northern Texas.

The residual dissipation term behaved erratically in time, ranging from over 21 watts  $m^{-2}$  on March 8 to a "negative" dissipation rate of over 29 watts  $m^{-2}$  on March 10. A further discussion and interpretation of this phenomenon will be found in Chapter VI. If an average over the volume for all days is taken, a mean rate of dissipation of 1.1 watts  $m^{-2}$  follows.

For comparison with the values computed here, table 5.2 indicates a range of values for frictional dissipation in the atmosphere above the boundary layer. Values by Kung (1969) are for the annual mean, and are presented in two layer thicknesses for comparison with the values computed by Trout and Panofsky (1969) in the upper troposphere. The value indicated by (\*) is an average over time of the residual dissipation computed here in pressure coordinates; the value

shown by (†) is an average of the direct calculation of dissipation for four days computed here in isentropic coordinates.

Table 5.2. Frictional dissipation in the free atmosphere

Author	Layer	Watts m <sup>-2</sup>
Kung (1969)	750-70 mb	2.28
	25,000-40,000 ft	1.28
Trout and Panofsky (1969)	25,000-40,000 ft	1.32
Ellsaesser (1969)	700-100 mb	1.44
Holopainen (1963)	900-200 mb	6.2
Jensen (1961)	925-100 mb	0.92
(*)	775-75 mb	1.09
(†)	700-250 mb	5.10

Frictional Dissipation in Isentropic Coordinates

A direct calculation of frictional dissipation in pressure coordinates leads to spurious results because of the nature of the stress gradient. Consequently, a computation of D in isentropic coordinates was undertaken. The stress computations in this coordinate system also serve as a check on the previous calculations, which were performed in a pressure coordinate system.

The equations of motion for isentropic surfaces are

$$\frac{du}{dt} = - \frac{\partial M}{\partial x} + fv + F_{x,\theta} \tag{5.4}$$

$$\frac{dv}{dt} = - \frac{\partial M}{\partial y} - fu + F_{y,\theta} \tag{5.5}$$

where  $M$  is the Montgomery stream function. If no appreciable vertical mass fluxes take place, diabatic effects are small, and if condensation or evaporation are minimal, motion may be considered adiabatic. For the cases investigated here, these conditions were applied to the use of the Montgomery stream function but not to the inertial term. In the transformation to isentropic coordinates, it has been assumed that

$$u_z = u_p = u_\theta$$

and

$$v_z = v_p = v_\theta .$$

The frictional dissipation takes the form

$$D_\theta = \vec{V}_{2,\theta} \cdot \vec{F}_{2,\theta} , \quad (5.6)$$

where the subscript  $\theta$  indicates computations in isentropic coordinates.

The direct calculation of dissipation, through a layer from about 700 mb to 250 mb, yielded  $5.1 \text{ watts m}^{-2}$  when averaged over all levels for the four time periods.

The vertical profiles of zonal shearing stress calculated in isentropic coordinates and presented in Figure 5.5 approximate those shown in Figure 3.2 for the pressure coordinate system. Using the convention of equating stress to vertical eddy flux of momentum, the profile for 0000 GMT March 9 exhibits the same vertical flux divergence patterns as 1800 GMT March 8. The vertical flux convergences at 0000 GMT March 10 and 11 were lower when calculated in the isentropic coordinates than those computed in pressure coordinates for 1800 GMT

March 9 and 10 respectively; the two coordinate systems reach good agreement for 0000 GMT March 12 and 1800 GMT March 11, 1969.

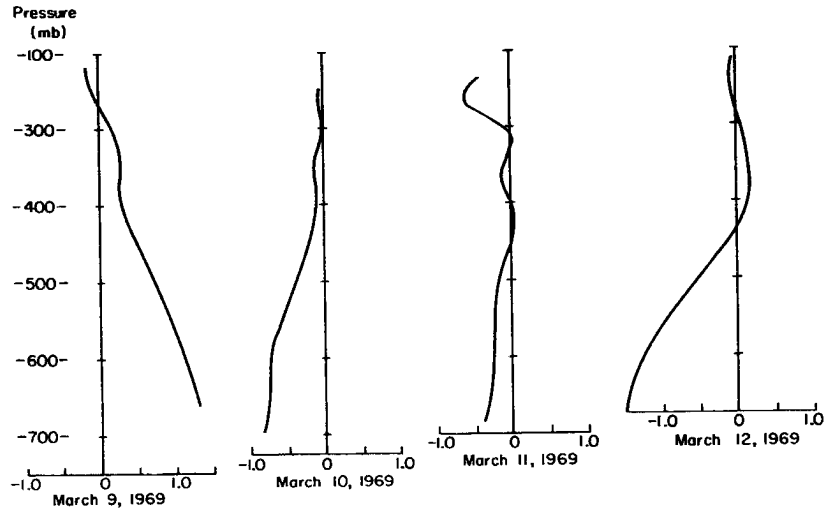


Figure 5.5. Vertical profiles of stress ( $\bar{\tau}_{x,\theta}$ ) in units of  $\text{kgm m}^{-1} \text{sec}^{-2}$  for 0000 GMT on days indicated, computed in isentropic coordinates. Multiply by 10 to obtain  $\text{dynes cm}^{-2}$ .

## VI. INTERPRETATION OF COMPUTATIONAL RESULTS

The large zonal stress gradients calculated for March 9-12, 1969 indicated a vertical flux on subgrid scales against the momentum gradient. Concurrently, the generation and dissipation of kinetic energy underwent a change from large positive values on March 8 to larger negative values on March 10, becoming positive on March 11 and 12 again. The counter-gradient flux became most intense when the broad uniform westerly flow entering the southwestern United States strengthened and developed a high-velocity jet maximum over Arizona and New Mexico.

The abrupt reversal in the direction of vertical flux of zonal momentum as indicated by computed shearing stresses (see Figure 3.2) accompanied the appearance of large areas of wave structure photographed during the Apollo IX flight on March 9, 1969. Unfortunately no cloud pictures were taken March 10, but photographs of the southwestern United States on March 11 and 12 indicated that the wave population had diminished prior to 1800 GMT March 11, 1969. The life cycle of the wave population can be viewed as parallel to an "energy generation cycle" exhibited in Table 5.1, suggesting a relationship between the subgrid-scale waves and the synoptic-scale energy computations.

### Momentum Transport

Momentum flux down the gradient on scales from centimeters to kilometers can be represented by exchange coefficients and is generally known as "K-type" transfer, or Fickian diffusion. Cumulus clouds, while they may transport heat against the gradient of potential

temperature, also act to redistribute momentum by turbulent processes down the gradient; cumulus processes do not, however, exhibit a functional dependence on the mean wind shear.

Momentum, however, can be transported against the gradient, contrasting with the transport of passive scalars. This phenomenon is sometimes called "negative viscosity" and has become the object of increasing interest in the past few years (Starr, 1968). The stably stratified atmosphere over the southwestern United States on March 8, 9, and 10, 1969 contained substantial shears in the upper half of the tropopause, effectively preventing upward turbulent vertical flux of zonal momentum by eddy mixing. In such regions where eddy turbulent momentum transport is inhibited, the transfer may plausibly be fulfilled by internal wave mechanisms (Stewart, 1969).

In a stable atmosphere over mountainous terrain, turbulence and internal gravity waves coexist; a nonlinear coupling between them causes energy to be exchanged between waves and turbulent eddies. The effects of such small-scale mechanisms on the synoptic-scale circulation are poorly understood (Sawyer, 1959). Perturbations in a stably-stratified atmosphere caused directly by topography include small-scale turbulence in the lower troposphere and gravity oscillations which may extend upwards as far as the stratosphere. The gravity waves, often with very large displacements over mountainous terrain, sometimes form into trains of lee waves. Large shearing stresses associated with the waves in stable layers extend upward into the high troposphere; it is generally believed that these stresses excite gravity waves which propagate vertically. These waves transport momentum and energy upward

or downward without concomitant mass transport except where shorter "breaking" waves, or billows, may occur, superimposed on the longer waves.

Mountainous, irregular terrain probably constitutes the main mechanism by which internal gravity waves are initiated and develop in the streamflow. Bretherton (1969a; 1969b) estimated that the upward transport of horizontal momentum associated with such internal gravity waves could be quite large, possibly changing the characteristics of the mean flow to great heights.

Since waves interact with turbulence weakly in a nonlinear way, and only under certain restrictive conditions, it is admissible to consider waves initially as distinct from turbulence even though they are usually present together (Busch, 1969). A simple mathematical development of gravity waves presented here will aid in the explanation of the computational results given in the three previous chapters. The development (Eliassen and Palm, 1960) allows a vertical shear of the horizontal wind and can include a non-uniform basic current; terms for buoyant energy and vertical transport of energy and horizontal momentum follow.

The perturbation equations assume a piezotropy coefficient

$$\gamma = \frac{d\rho}{dp}, \quad (6.1)$$

in which  $d$  is the individual differential;  $\gamma^{-\frac{1}{2}}$  is the velocity of sound. The flow is first taken as a straight current parallel to the  $x$ -axis and a function of height  $U(z)$ . The hydrostatic relationship between pressure and density becomes

$$\frac{d\rho_o}{dz} = -\rho_o g \quad (6.2)$$

when the subscript  $_o$  represents the basic current characteristics. The density stratification

$$\Gamma = \frac{d\rho_o}{d\rho_o} \quad (6.3)$$

leads to a vertical density gradient in the form

$$\frac{d\rho_o}{dz} = \Gamma \frac{d\rho_o}{dz} = -\Gamma g \rho_o . \quad (6.4)$$

The Brunt-Väisälä (buoyancy) frequency ( $v_o$ ), representative of the static stability of the flow, is then

$$v_o^2 = (\Gamma - \gamma)g^2 . \quad (6.5)$$

This wave motion behaves independently of  $y$  and is constrained to act in the  $xz$ -plane with a vertical displacement  $z'$ , perturbation velocities  $u'$  and  $w'$ , pressure  $p$ , and density  $\rho$ . Rearranging and discarding all but first-order terms, the following results:

$$\rho = \frac{v_o^2}{g} \rho_o z' + \gamma p . \quad (6.6)$$

Substituting this expression for density into the equations of motion, they become, for stationary flow,

$$\rho_o U \frac{\partial u'}{\partial x} + \rho_o \frac{\partial U}{\partial z} w' + \frac{\partial p}{\partial x} = 0 \quad (6.7)$$

and 
$$\rho_o U \frac{\partial w'}{\partial x} + \rho_o v_o^2 z' + \frac{\partial p}{\partial x} + \gamma g \rho = 0 . \quad (6.8)$$

The continuity equation is

$$\frac{\partial u'}{\partial x} + \frac{\partial w'}{\partial z} - \gamma g w' + \frac{\gamma U}{\rho_0} \frac{\partial p}{\partial x} = 0, \quad (6.9)$$

where  $w' = U \frac{\partial z'}{\partial x}.$  (6.10)

After multiplying the equations of motion by  $u'$  and  $w'$  respectively and the equation of continuity by  $p$ , and adding, the wave equation is

$$\frac{\partial}{\partial x}(EU + pu') + \frac{\partial}{\partial z}(pw') = -\rho_0 \frac{\partial U}{\partial z} u'w'. \quad (6.11)$$

The right-hand side of (6.11) represents a source of wave energy through the conversion of kinetic energy of the mean current and can be either positive or negative. The definition

$$E \equiv \frac{1}{2} \rho_0 \{ [(u')^2 + (w')^2] + v_0^2 z'^2 + \gamma \rho_0^{-2} p^2 \} \quad (6.12)$$

sets  $E$  equal to the wave energy per unit volume;  $\frac{1}{2} \rho_0 [(u')^2 + (w')^2]$  is the kinetic part and  $\frac{1}{2} \rho_0 (v_0^2 z'^2 + \gamma \rho_0^{-2} p^2)$  stands for the available potential and internal energies.

The first term on the left-hand side of (6.11) measures the horizontal flux divergence through vertical boundaries; the second measures the vertical divergence through horizontal surfaces. Multiplying by  $(\rho_0 U u' + p)$  and integrating over  $x$  from  $-\infty$  to  $+\infty$ , (6.7) becomes

$$\int_{-\infty}^{\infty} p w' dx = -U \rho_0 \int_{-\infty}^{\infty} u' w' dx; \quad (6.13)$$

integration of (6.11) with respect to  $x$  from  $-\infty$  to  $+\infty$  yields

$$\frac{d}{dz} \int_{-\infty}^{\infty} p w' dx = - \frac{\partial U}{\partial z} \rho_0 \int_{-\infty}^{\infty} u' w' dx , \quad (6.14)$$

for the case of lack of resonance.

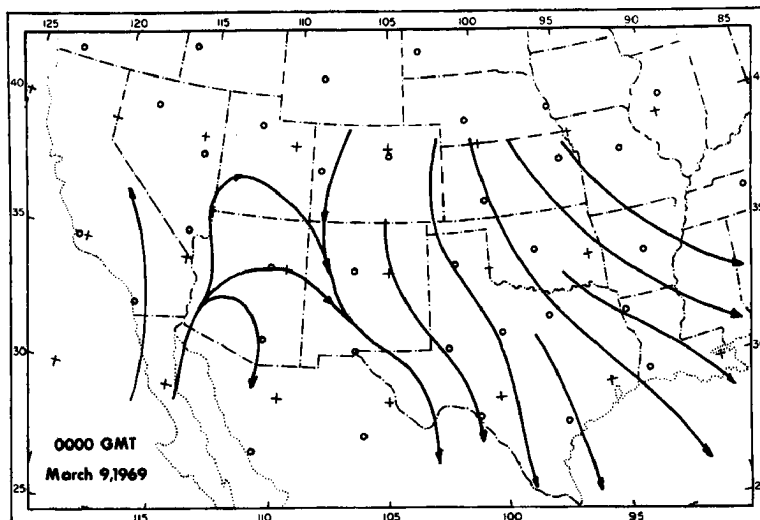
Thus, in a layer in which  $U \neq 0$ , the vertical flux of energy varies with height in proportion to  $U$ ; sources of wave energy vary with height in proportion to  $\partial U / \partial z$ . Further, if  $U$  is everywhere positive in the layer, the vertical flux of energy takes a direction opposite to the vertical flux of momentum; i.e., if energy is transferred downward, momentum flows upward by wave action.

In Fourier representation, it can be shown that, where  $U \ll \gamma^{-\frac{1}{2}}$ , for a single component in mountain waves where  $U \neq 0$ ,

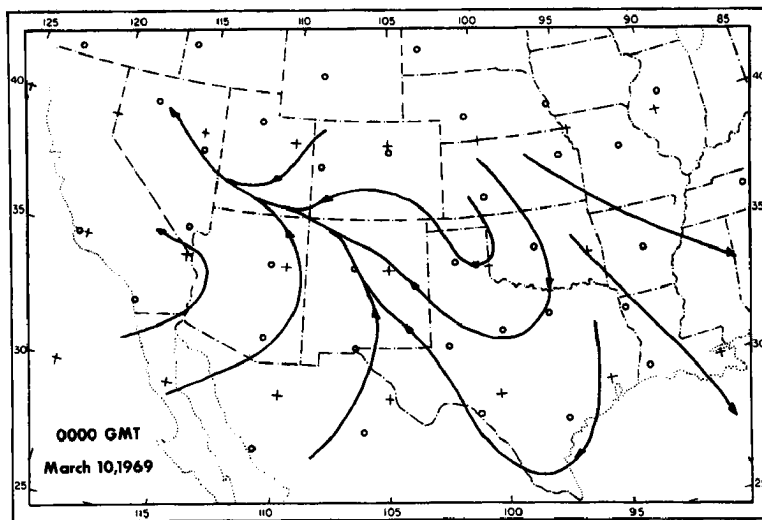
$$\overline{p w'} = \frac{U \rho_0}{k^2} \overline{\frac{\partial w'}{\partial x} \frac{\partial w'}{\partial z}} \quad (6.15)$$

depends upon the tilt of the waves with height. If the wave axis tilts downstream with height, perturbation energy flows downward and momentum upward; if  $U$  increases with height, the kinetic energy of the wave motion converts into mean motion. Conversely, if the axis tilts upstream with height, perturbation energy flows upward, momentum downward, and kinetic energy of mean motion converts to wave energy.

The downstream tilt with height of the wave axis is compatible with easterly air flow in the lower levels and westerly flow at upper tropospheric levels; upstream tilt follows with westerly flow extending upward from the surface layers (R. S. Scorer, personal communication). The streamline analysis of planetary boundary-layer winds (Figure 6.1a)



(a)



(b)

Figures 6.1(a) and (b). Streamline analysis for flow in the lowest 100 mb of the atmosphere for 0000 GMT March 9 (a) and March 10 (b), 1969.

for 0000 GMT March 9, 1969 exhibits the westerly flow typical of upstream tilt; the analysis for 0000 GMT March 10, 1969 shows the contrasting easterly flow in the lowest 100 mb of the atmosphere over western Texas and New Mexico (Figure 6.1b). In these analyses the available 1800 GMT March 8 and 1800 GMT March 9 pilot balloon data were added to the 0000 GMT March 9 and 000 GMT March 10 rawinsonde data, respectively.

The easterly boundary-layer flow resulted from a southward plunge of cold air east of the Rocky Mountains and corresponded to a negative zonal shearing stress in the atmosphere (upward momentum transfer). Westerly flow at 0000 GMT March 9 corresponded to a positive zonal shearing stress and downward transfer, as reported in Chapter III.

#### Zonal Shearing Stresses

Zonal shearing stresses in the atmosphere at the top of the planetary boundary layer averaged as high as  $2.5 \text{ newtons m}^{-2}$ , or  $25 \text{ dynes cm}^{-2}$ , on occasion, when measured in a pressure coordinate system. Local values over the high mountains in central and east-central New Mexico reached as much as four times the average. The stresses for the same period computed in isentropic coordinates were somewhat smaller but of the same order of magnitude and of the same sign.

Current literature on surface stress values allows a wide latitude for comparison but considerably fewer values are available for the free atmosphere. Riehl and Baer (1964) computed the February, 1960, mean surface stress over the North American mountain region at about

15 dynes  $\text{cm}^{-2}$ . The region for their computations covered but 2.5% of the polar cap north of  $28^\circ$  N latitude and contributed 25.8% of the total stress for the cap. The magnitude of the mean low-level zonal stresses computed here approximates the magnitude of the values computed by Riehl and Baer. Riehl and Baer also found negative zonal stresses in some instances.

Blumen (1965), using a wave model for airflow over a line of equally-spaced circular mountains, achieved a surface stress of 16 dynes  $\text{cm}^{-2}$  with a wave amplitude of 300 meters. Since the stress due to wave drag increases according to the square of the amplitude, an amplitude of about 800 meters in the same model would approximate the stress computed over central New Mexico at 1800 GMT March 10, 1969. Thus, the stress values presented in Figure 3.2 are on the same order as stress over rugged terrain. Sawyer (1959) estimated that about one-half of the stress is in the lowest 3 km of the atmosphere with the remainder distributed over the upper troposphere and the stratosphere. His computation of wave drag in a flow of  $20 \text{ m sec}^{-1}$  over a 300 m barrier indicated a stress of 7.6 dynes  $\text{cm}^{-2}$  at the surface. Surface frictional stress values listed by Sawyer for various types of terrain covered more than one order of magnitude.

Vorticity contributions by stresses in the atmosphere (see Table 4.1, last column) reached  $4 \times 10^{-6} \text{ kgm m}^{-2} \text{ sec}^{-2}$  ( $4 \times 10^{-7} \text{ gm sec}^{-2} \text{ cm}^{-2}$ ) on March 9, 1969, reducing the vorticity at 1800 GMT March 8 and increasing it at 1800 GMT March 9. This compared favorably with vorticities due to the wave drag calculated by Sawyer (1959) of  $1.5 \times 10^{-7} \text{ gm sec}^{-2} \text{ cm}^{-2}$  ( $1.5 \times 10^{-6} \text{ kgm m}^{-2} \text{ sec}^{-2}$ ). In the two cases

selected here for vorticity budget computations, the stress term and the twisting term were sufficiently large to demand inclusion; ignoring either of these terms would have led to substantial difficulty in establishing vorticity balance. The vorticity budget calculations indicated the consistency of the stress gradient computations discussed in Chapter III.

#### Kinetic Energy and the Energy Cycle

The kinetic energies calculated for March 8, 9, and 10, 1969 strongly suggested a cycle in the generation of kinetic energy. A total dissipation of about  $21 \text{ watts m}^{-2}$  would have been required to balance the energy budget for 1800 GMT March 8; a generation, or "negative dissipation" of about  $29 \text{ watts m}^{-2}$  was needed for 1800 GMT March 10 (see Table 5.1). While the residual (dissipation) displayed sizeable error limits, the sign of the residual was established. The role of internal gravity waves in the energy cycle was investigated through a calculation of the buoyant potential energy stored in the density variations of the waves.

A comparison of the Bolgiano and the Lumley-Shur buoyancy subrange theories by O. M. Phillips (1967) treated the basic assumptions of these theories. If the mean density distribution is statically stable, the working of vertical motions against buoyant forces can act as a sink on the subgrid scale to the energy of the mean and turbulent flow. When the areal extent of the wave population reaches the synoptic scale, it is reasonable to expect that the available potential energy in the waves will have an impact on the kinetic energy budget.

The removal of energy from a turbulent flow field, and the transformation of the energy, has been treated by Bolgiano (1962). He assumed adiabatic processes in developing the equations of motion for mountain-perturbed flow in stable stratifications. He introduced potential density ( $\rho = p/R\theta$ ) and density-normalized pressure; thus the adiabatic assumption became a conservation statement for the potential density. Nonlinear interactions were neglected and a solution made for natural modes of internal gravity waves for steady processes. The following relationship obtains:

$$\frac{\partial}{\partial t} \left( \frac{1}{2} \overline{u'_i u'_i} \right) = - \overline{u' w'} \frac{\partial U}{\partial z} - u'_i \frac{\partial}{\partial x_i} \left( \frac{1}{2} \overline{u'_i u'_i} + p' \right) - \frac{g}{\rho_0} \overline{(w' \rho')} - \epsilon, \quad (6.16)$$

where  $u'_i$ ,  $\rho'$ , and  $p'$  are local deviations at  $x_i$ .

The time change in turbulent kinetic energy (left-hand side) depends upon (1) production through interaction of the shearing stress and the shear of the mean flow; (2) the action of gravitational forces (third term on the right-hand side); and (3)  $\epsilon$ , the dissipation due to viscous forces. The second term on the right-hand side accounts for interaction between the components of motion.

The gravitational term measures the abstraction of kinetic energy from the turbulent field by work done against the buoyant forces. If the energy reaches steady state, the first term on the right-hand side of (6.14) equals the storage in the buoyancy term and the viscous dissipation. The storage term represents potential energy that would

be released by the return of all fluid elements to equilibrium level without loss of buoyancy. Per unit mass, this is

$$\phi = -\frac{1}{2} \frac{g}{\rho_0} \frac{(\rho')}{\overline{d\rho}/dz} \quad (6.17)$$

where  $\overline{d\rho}/dz$  represents the vertical gradient of the mean potential density;  $\rho'$  is the density deviation from the base density  $\rho_0$ . When the wave structure erodes by the action of breaking waves, or billows, a certain amount of mixing in the region occurs. (6.17) corresponds to the buoyant potential energy in the third term on the right-hand side of (6.12).

#### Potential Energy of Waves

An approximation of the amount of potential energy contained in the density deviations of a wave population requires (1) an estimate of the areal coverage of the waves; (2) a knowledge of the atmospheric stabilities in the wave region, and (3) reasonable estimates of the wave amplitudes.

The Apollo IX photographs serve to give a first-order estimate of the wave population over western Texas and New Mexico. The area ABCFED in Figure 2.3 exhibits wave structure at two levels: waves at A and billows at 116W 35 25N can be seen in Figure 2.4; and waves are apparent at A in Figure 2.5. Longer lee waves at A in Figure 6.2 extend downstream from the jet stream cloud into western Texas where they appear at A in Figure 6.3. Billow clouds with a wavelength of about 500 m are superimposed on the longer waves at B and upstream

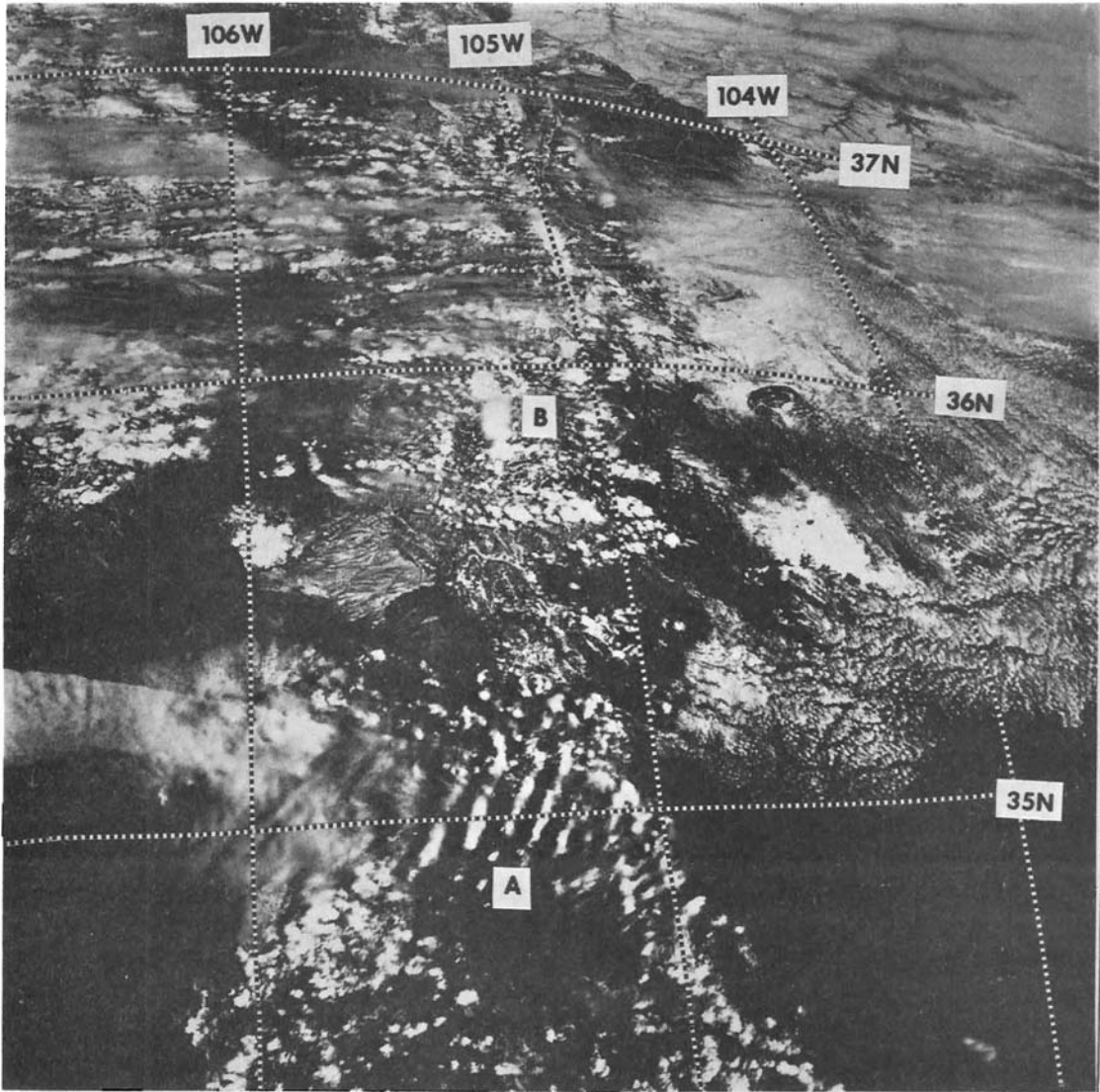


Figure 6.2. Apollo IX photograph No. 3447, taken at approximately 1804 GMT March 9, 1969. Lee wave clouds are visible at A; a cap cloud covers the mountain ridge at B.

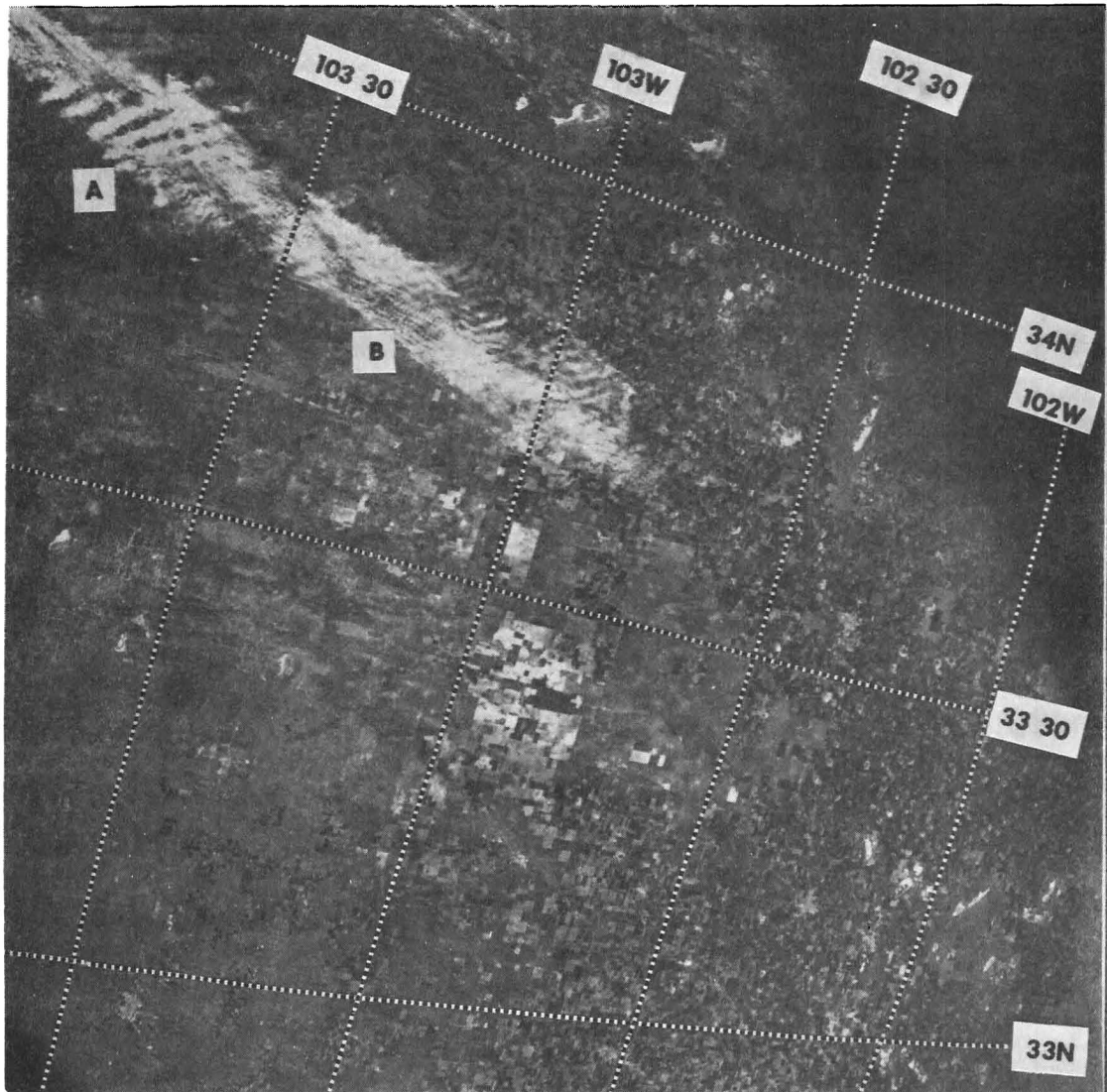


Figure 6.3. Apollo IX photograph No. 3294, taken at approximately 1805 GMT March 9, 1969. Wave clouds at A are in the lee of the mountains; billows at B are superimposed on the longer waves.

displacement of 350 m was assumed and the Winslow and Albuquerque soundings taken at 1200 GMT March 9 (approximately six hours prior to the photographic mission for Apollo IX for that day) were selected. An examination of the moisture available in the stable layers at Albuquerque indicated a required lifting of 200 m for condensation.

The Winslow and Albuquerque soundings were divided into several layers having uniform lapse rates, and (6.17) was applied to each layer from 800 mb to the tropopause. The computed potential energy in the wave structure totaled  $6.7 \times 10^5$  joules  $m^{-2}$  at Winslow and  $9.3 \times 10^5$  joules  $m^{-2}$  at Albuquerque, or an average of  $8.0 \times 10^5$  joules  $m^{-2}$  ( $8.0 \times 10^8$  ergs  $cm^{-2}$ ). The 21 watts  $m^{-2}$  indicated as an energy residual at 1800 GMT March 8 could supply the  $8.0 \times 10^5$  joules for 30% of the study region in a period of 3.2 hours.

#### Dissipation of Wave Energy

The amplitudes of internal gravity waves will continue to grow as long as energy is supplied, until the wave motion becomes potentially unstable. Once instability occurs, patches of turbulence will result in loss of energy through viscous dissipation to heat (O. M. Phillips, 1967). If energy is no longer continuously supplied to the internal gravity waves the motion will remain stable.

Mesoscale features such as gravity waves have been observed to be stationary for periods of one or several hours (Reed, 1969). Lee waves often remain in place long enough for two or more aircraft penetrations (Vergeiner and Lilly, 1969). As a means of estimating the rate at which the energy supply exceeded stability levels in the

internal gravity waves and of determining the approximate period of persistence of the wave population, a synopsis of the clear air turbulence reports was prepared.

On March 8 during the time interval from 1800 to 2000 GMT, light to moderate turbulence was reported over southeastern New Mexico and western Texas. Using Trout and Panofsky's (1969) values of about  $60 \text{ cm}^2 \text{ sec}^{-3}$  over 50 mb of the mid-troposphere, this represented 3 watts  $\text{m}^{-2}$  over an area approximating 10% of the study region, or 0.3 watts  $\text{m}^{-2}$  averaged over the entire region.

A mixture of light, moderate, and severe clear air turbulence prevailed over central and southern New Mexico, southeastern Arizona, and extreme western Texas at 1800 to 2000 GMT March 9. Using a value of  $85 \text{ cm}^2 \text{ sec}^{-3}$  over 50 mb, again at mid-troposphere, this amounted to 4.2 watts  $\text{m}^{-2}$  over about 30% of the region, or 1.3 watts  $\text{m}^{-2}$  average dissipation.

The turbulence diminished to light-to-moderate over southeastern Arizona and southern New Mexico on March 10, becoming light and patchy over central New Mexico and western Texas on March 11 and 12.

The turbulence estimates indicate that a maximum transfer of energy to the gravity waves occurred on March 9, with lesser amounts on the succeeding three days. The total  $\epsilon$ -type energy dissipation in the turbulent areas was considerably less than the energy generation rate calculated for 1800 GMT March 8, 1969.

An average over area and time of the residual in the kinetic energy calculation might be expected to yield a reasonable rate of energy dissipation to heat at each level in the atmosphere if no

mountains, suggesting a downwind tilt with height of the vertical wave axes. Mean values of the energy budget residual at standard levels indicated a flux of kinetic energy downward into the troposphere when zonal momentum was transported upward.

Based on Apollo IX photographs, the areal coverage of gravity waves over the computational region was estimated at 30%. Winslow, Arizona and Albuquerque, New Mexico soundings at 1200 GMT March 9 were used to calculate the buoyant potential energy contained in the density deviations of the waves. This energy totaled  $8 \times 10^5$  joules  $m^{-2}$  in the wave area below the tropopause for an estimated mean particle displacement of 350 meters. While the estimation of this energy could be in error by a factor of two or three, the energy sink in the extensive wave population was of the same order of magnitude as the synoptic scale energy generation and divergence.

Clear air turbulence intensity reached a maximum during the greatest areal coverage of waves, decreasing in intensity as the kinetic energy generation diminished and as the wave population reduced. The "epsilon" energy loss to heat due to viscous forces was estimated to be nearly one order of magnitude smaller than the synoptic-scale energy generation during the extensive wave coverage, diminishing gradually as the wave population decreased.

### Conclusions

Through the action of large areas of gravity waves with a downstream tilt of their vertical axes, a substantial countergradient flux of zonal momentum can converge in the upper troposphere and

lower stratosphere to maintain or increase tropopause-level flow against frictional dissipation to heat. The buoyant potential energy contained in extensive gravity wave populations can be large enough to act as an energy sink of the same order of magnitude as the synoptic-scale kinetic energy generation.

#### Recommendations

The study described here supports the feasibility of acquiring mesoscale meteorological data from a manned spacecraft over an area sufficiently large to measure the mesoscale interaction with synoptic scale phenomena. Trained observers on board spacecraft, orbiting the earth at altitudes of 200 to 300 kilometers, have the advantage of being able to recognize meteorological processes in the context of several scales of motion, and of selecting areas for photography. The amount of data obtained can be held commensurate with operational needs and investigational purposes without overwhelming data processing facilities with a great deal of extraneous information.

In contrast to the fixed capabilities of most unmanned weather satellites, the manned spacecraft would be capable of operational flexibility. High-resolution cameras in precision mountings could be programmed to record particular areas of interest in sufficient detail to provide near real-time information for aircraft flights in areas of wave clouds and accompanying clear air turbulence. Parameterized relationships between atmospheric scales of motion could be researched and incorporated into numerical models for forecasting purposes.

## APPENDIX A

### Error Analysis

The error analysis performed on the kinetic energy terms makes use of two rules:

Rule A. The percentage error of the product of numbers is the sum of the percentage errors of the variable quantities entering into the computation.

Rule B. The numerical error of a sum is the sum of the numerical errors of the individual quantities.

The percentage error of each term on the right-hand side of equation (5.1) was arrived at through a logarithmic differentiation of the variable quantities in each term. Thus the error in the first term on the right-hand side was

$$\frac{2\delta v}{v} , \quad (\text{A.1})$$

where it was assumed that the velocity error  $\delta v$  was  $2 \text{ m sec}^{-1}$  and the mean velocity  $v$  was  $40 \text{ m sec}^{-1}$ . The result was an error of 10%.

The second term in (5.1) contains the product  $Kc_n$ ; the error was then

$$\frac{2\delta v}{v} + \frac{\delta c_n}{c_n} \quad (\text{A.2})$$

A mass balance was imposed on each layer for each time period, reducing the error in the normal velocity component  $c_n$ . Therefore  $\delta c_n$  was taken as  $1 \text{ m sec}^{-1}$ , and the mean  $c_n$  as  $25 \text{ m sec}^{-1}$ ; the error was  $(10 + 4) \%$ , or 14%.

The product of variables in the third term in (5.1) is K ;  
the error becomes

$$\frac{2\delta v}{v} + \frac{\delta\omega}{\omega} \quad . \quad (A.3)$$

Assuming  $\delta\omega/\omega$  at about 8%, the error in this term was taken to be  
(10 + 8)%, or 18%.

The last term in (5.1) contains the product  $\vec{V} \cdot \nabla z$ , with the  
error

$$\frac{\delta v}{v} + \frac{\delta(\nabla z)}{\nabla z} \quad . \quad (A.4)$$

Estimating  $\delta(\nabla z)$  at 5 meters and using a mean  $\nabla z$  of 120 meters yields  
an error of (5 + 4)%, or 9%.

In table 5.1 the totals (integrated over pressure) for each  
term in the energy budget were multiplied by the appropriate per-  
centage to obtain the numerical error; the individual errors were added  
to give the error shown for the residual (dissipation).